REPORT DOCUMENTATION PAGE

Form Approved
OMB No. 0704-0188

1. REPORT DATE *(DD-MM-YYYY)*	2. REPORT TYPE	3. DATES COVERED *(From - To)*
01/11/2018	Final Technical Report	June 01 2016 - Dec 30 2017

4. TITLE AND SUBTITLE
Finite-Element Barotropic Model for the Indian and Western Pacific Ocean Basin: Tidal Model-Data Comparisons and Sensitivities

5a. CONTRACT NUMBER

5b. GRANT NUMBER
N00014-15-1-2623

5c. PROGRAM ELEMENT NUMBER

6. AUTHOR(S)
Pringle, William, J
Suhardjo, Andika
Wirasaet, Damrongsak
Westerink, Joannes, J
Kennedy, Andrew, B

5d. PROJECT NUMBER

5e. TASK NUMBER

5f. WORK UNIT NUMBER

7. PERFORMING ORGANIZATION NAME(S) AND ADDRESS(ES)
Environmental Fluid Dynamics Group
Department of Civil and Environmental Engineering and Earth Sciences,
University of Notre Dame,
Notre Dame, IN, 46656, USA

8. PERFORMING ORGANIZATION REPORT NUMBER

9. SPONSORING/MONITORING AGENCY NAME(S) AND ADDRESS(ES)

10. SPONSOR/MONITOR'S ACRONYM(S)

11. SPONSOR/MONITOR'S REPORT NUMBER(S)

12. DISTRIBUTION/AVAILABILITY STATEMENT
Approved for Public Release; distribution is Unlimited

13. SUPPLEMENTARY NOTES

14. ABSTRACT
We develop a 9.6 million node unstructured grid finite-element barotropic fully hydrodynamic model in order to understand the shallow-water dynamics of the Indian Ocean and Western Pacific Ocean basins down to sub-kilometer scale at the coast. Tidal model-data comparisons against tide gauges and a global data-assimilated model are conducted in order to identify the capabilities and limitations of our model. The average root-mean-square (RMS) discrepancies of the total free surface at coastal tide gauges is 14 cm, ~3 cm smaller than the data-assimilated model. Sensitivities related to lateral boundary conditions, bathymetry, and dissipative dissipative processes are explored.

15. SUBJECT TERMS
finite-element, unstructured grid, barotropic tides, bathymetry, internal tide generation, bottom friction

16. SECURITY CLASSIFICATION OF:			17. LIMITATION OF ABSTRACT	18. NUMBER OF PAGES	19a. NAME OF RESPONSIBLE PERSON
a. REPORT	b. ABSTRACT	c. THIS PAGE			Joannes J. Westerink
			UU	47	19b. TELEPHONE NUMBER *(Include area code)* +1-574-631-6475

Finite-Element Barotropic Model for the Indian and Western Pacific Ocean Basin: Tidal Model-Data Comparisons and Sensitivities

William J. Pringle[1] Andika Suhardjo Damrongsak Wirasaet
Joannes J. Westerink[2]
Andrew B. Kennedy

Environmental Fluid Dynamics Group
Department of Civil and Environmental Engineering and Earth Sciences
University of Notre Dame
Notre Dame, IN, 46656, USA

January 11, 2018

[1]Corresponding author: wpringle@nd.edu
[2]Principal Investigator: jjw@nd.edu

Abstract

We develop a 9.6 million node unstructured grid finite-element forward barotropic model in order to understand the shallow water dynamics and dissipation mechanisms of the Indian and Western Pacific Oceans down to sub-kilometer scale at the coast. Tidal model-data comparisons against tide gauges and a global data-assimilated tidal model are conducted in order to identify the capabilities and limitations of our model. The average root-mean-square (RMS) discrepancies of the total free surface at coastal tide gauges is 14 cm, ~3 cm smaller than the data-assimilated model. Sensitivities related to lateral boundary conditions, bathymetry, and dissipative processes are explored. Lateral boundary conditions were found to induce global resonant effects on the lunar semi-diurnal modes when poorly placed elevation specified boundary conditions were used. This problem is largely resolved by using an absorption-generation layer at the boundary, although errors may persist in the flux component obtained from data-assimilated tidal models. Parameterization of internal tide dissipation is identified as the most important aspect to control deep water solutions, and reduce the RMS discrepancies of the entire system. Two forms of this parameterization were presented and their spatial distributions of dissipation were compared. Bathymetry has a negligible effect on the tidal solutions in deep water, but local high-resolution bathymetry results in significant reductions to the average RMS discrepancies on the continental shelf (26%) and at the coast (30%). Implementing a spatially varying bottom friction coefficient based on sediment types decreases the average RMS discrepancy at the coast by 9% predominantly due to its positive effects in the Yellow Sea. The model is shown to capture a large amount of the tidal physics and has the potential for application to a wide range of shallow water problems in the region.

Keywords: finite-element; unstructured grid; barotropic tides; bathymetry; internal tide generation; bottom friction

1 Introduction

The Indian Ocean and Western Pacific Ocean (IndWPac) represent approximately 30% of the surface area of the world ocean, are interconnected by marginal seas such as the Java, Timor, Banda, Andaman and Arafura Seas, and are separated by the intricate island chains of Indonesia and the Philippines. Major ports and cities are located in the northern parts of both the Indian Ocean (Dubai, Karachi, Mumbai, Colombo) and the Western Pacific Ocean (Hong Kong, Shanghai, Tokyo, Singapore), representing a significant portion of the world's economy and human population.

Given the rapidly changing coastal zone in much of the IndWPac region, the development of a large-scale comprehensive barotropic model is needed to advance modeling capabilities of tides, wind driven surge and circulation and their nonlinear interactions nearshore. We aim to be on par with contemporary models in other regions receiving significant attention such as the western North Atlantic (e.g. Westerink et al., 2008; Bunya et al., 2010; Kerr et al., 2013). The challenge of the IndWPac region is that it is more complex in its geometry, topography (e.g. it contains many interconnected shallow seas and island chains) and associated hydrodynamics than the Western North Atlantic region.

To model the dynamics at coastal locations within the IndWPac region, all processes and exchanges from ocean basin scale to harbor inlet scale, must be appropriately represented. Coarse resolution global models (e.g. Egbert, Ray, and Bills, 2004; Green and Nycander, 2013; Buijsman et al., 2015) capture the large-scale dynamics but they may miss nearshore features and important nonlinearities. Conversely, carefully calibrated local domain hydrodynamic models can accurately capture local effects (e.g. Green and David, 2013; Zu, Gan, and Erofeeva, 2008, in South China Sea), but they may miss basin-scale effects from offshore and are restricted by boundary conditions. A single unstructured grid finite-element model of the region is suitable because it can utilize varying resolutions to produce high fidelity coastal bathymetry of critical geographic and topographic features such as island chains, reef systems, and floodplain systems; provide connectivity to estuarine and harbor systems where most water level gauges are located and where dense coastal populations live; and capture key dynamics of a large regional domain.

To assess the capabilities and limitations of a large-scale finite-element barotropic model in the IndWPac region, model-data comparisons of the tidal elevations are investigated in this study. This can be achieved point-wise at tide gauges or regionally against global data-assimilative model atlases. Examples of the latter include TPXO (Egbert and Erofeeva, 2002), FES (Lyard et al., 2006), and NAO.99b (Matsumoto, Takanezawa, and Ooe, 2000). These models assimilate data from satellite altimetry and selected coastal tide gauges to accurately obtain estimates of the tidal elevation fields in terms of individual harmonic constituents. Modern data-assimilated models can achieve M_2 tidal wave root-mean-square errors (RMSE) of 0.5 - 0.7 cm versus deep-ocean bottom pressure recorder stations (Stammer et al., 2014). In contrast, M_2 RMSE ranges between 5.6 - 12.7 cm for purely hydrodynamic global models without data-assimilation (Stammer et al., 2014). However, non-assimilative forward models on large-domains can be applied to a wide variety of problems including wind, pressure and wave coupling effects, and may be used to conduct future forecasting and perturbation response analysis (Green and David, 2013), e.g. due to changing sea level, dredging operations, and land reclamation (Suh, Lee, and Kim, 2014).

Based on the model-data comparisons we aim to discern areas where a high-resolution model has advantages over coarser models and where lingering discrepancies remain. Moreover, a discussion on the major reasons for these is of great interest to inform future developments of coastal ocean models and their applications. This is achieved through assessment of the sensitivities of the various controls on the barotropic tidal dynamics (lateral boundary position, boundary condition implementation, bathymetry, and dissipative processes). For example, two global bathymetric databases

are compared, and high-resolution local bathymetric data is included where available to assess the potential of improved bathymetry facilitating improvements in the solution.

Regarding dissipative processes, significant progress has been made in reducing tidal elevation errors in deep water through parameterizations of tidal energy conversion from barotropic to baroclinic modes through internal tide generation over submarine ridges (Jayne and St. Laurent, 2001; Egbert, Ray, and Bills, 2004; Zaron and Egbert, 2006; Green and Nycander, 2013; Buijsman et al., 2015). This paper will refer to that physical process as *internal tide dissipation*, and will discuss the significance of its effects in the IndWPac region. In addition, spatially varying bottom friction coefficients are rarely considered in large-scale models. Instead, a canonical spatially constant coefficient is commonly applied (Lyard et al., 2006; Egbert and Erofeeva, 2002). However, changing the bottom friction coefficient has been shown to have positive effects regionally (Lefevre, Provost, and Lyard, 2000). We take a preliminary look at the effect of spatially varying coefficients that are based on local sediment types and hydrodynamics, an important consideration for the IndWPac domain where diverse sediment categories are present across wide and very shallow continental shelves.

To summarize, this paper describes the development of the IndWPac unstructured grid and hydrodynamic modeling system, built with state-of-the-art bathymetric datasets, absorptive boundary conditions, and parameterizations of internal tide and bottom friction dissipation. We analyze the sensitivity of the model to these four factors, and conduct model-data comparisons against both tide gauge records and a data-assimilated tidal model. The capabilities and limitations of the model are identified and discussed. Suggested areas of focus in order to advance barotropic coastal ocean models are highlighted.

2 Domain Definition, Bathymetry, and Unstructured Grid Development

Our basin-scale model includes the entire Indian Ocean, the western half of the Pacific Ocean, and the Southern Ocean between these extents. Specifically, the domain (Fig 1) lies between 17.9°E - 175.8°E longitude and 73.3°S - 62.7°N latitude covering an area of roughly 150 million km^2. There are two open ocean boundaries: a longitudinal parallel boundary running from nearby the Cape of Good Hope, South Africa to Antarctica; and a concave shaped boundary between the Bering Sea coast of Kamchatka Krai, Russia and Antarctica. The boundaries were chosen so that tidal amphidromic points and complications with the Aleutian, Hawaiian and New Zealand islands in the Pacific Ocean were avoided (an illustration on the effects of boundary placement is shown in §5.1).

The mesh is a triangular unstructured grid with resolution ranging from as large as 25 km in parts of the deep ocean down to 1 km along most coastlines (Fig 2). Additionally, resolution is as fine as 100 m in the ports and harbors of Hong Kong, Tokyo Bay and Osaka Bay. The grid contains a total of 9.6 million nodes and 18.8 million elements.

Development of the unstructured grid was achieved predominantly through an automated algorithm that we developed in-house based on the MATLAB DistMesh code (Persson and Strang, 2004). Resolution is varied through an edgelength (local grid resolution) function λ_E, defined as the minimum of three criteria:

$$\lambda_E = \min\left(\lambda_m + \alpha_d d, \quad \frac{T}{\alpha_w}\sqrt{gh}, \quad \frac{2\pi}{\alpha_s}\frac{h}{|\nabla h|}\right) \tag{1}$$

where λ_m is the nominal minimum edgelength, d is the distance from a node to the closest coastline boundary, T is the period of the M_2 tidal wave, h is the bathymetric depth, and α are the dimensionless user-defined coefficients for each criterion: distance from the coastline ($\alpha_d = 0.075$),

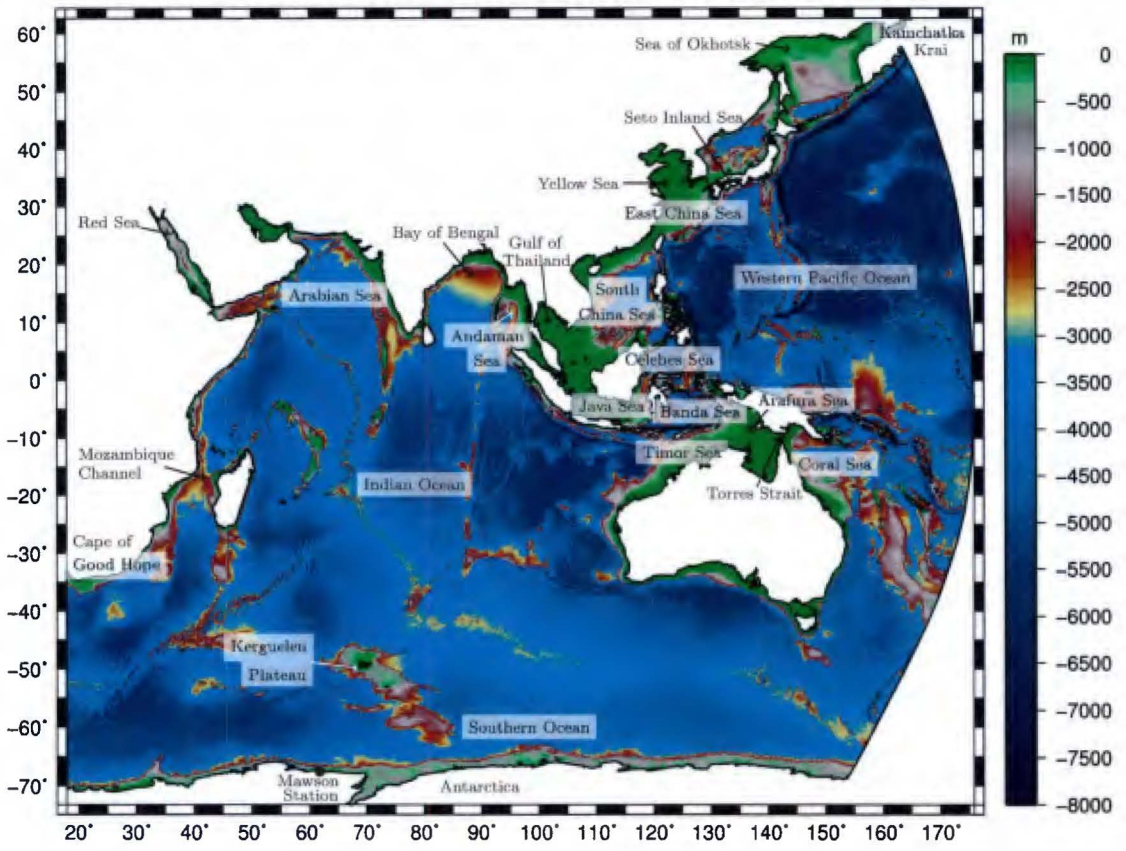

Figure 1: Bathymetric depths of the grid as interpolated from various sources (Table 1) using a cell-averaged approach.

wavelength ($\alpha_w = 600$), and topographic length scale ($\alpha_s = 30$). These criteria ensure that important bathymetric features are captured throughout the ocean in addition to obtaining higher resolution nearshore.

Model bathymetry is interpolated onto the grid from a number of sources in a specified order using an automated cell-averaging technique (Bilskie and Hagen, 2013) as summarized in Table 1. The adopted background bathymetry is the 1/120° SRTM30_PLUS global database combined with a synthetic realization of seafloor roughness along the abyssal hills (Goff and Arbic, 2010; Timko et al., 2017). The synthetic abyssal hill roughness is used because the effective resolution of the global altimetric based bathymetry is limited to >10 km in the deep ocean while ~1 km resolution is necessary to describe the required topographic roughness that generates internal tides converting barotropic energy into baroclinic energy (Goff and Arbic, 2010; Melet et al., 2013; Timko et al., 2017). In addition, to include depths under ice shelves in Antarctica we interpolate from the TPXO8 model bathymetry containing the Padman et al. (2002) dataset.

For shallower regions (in depths < 500 m) where the abyssal hill roughness is not important, we start by interpolating from the global 1/240° SRTM15_PLUS database which improves

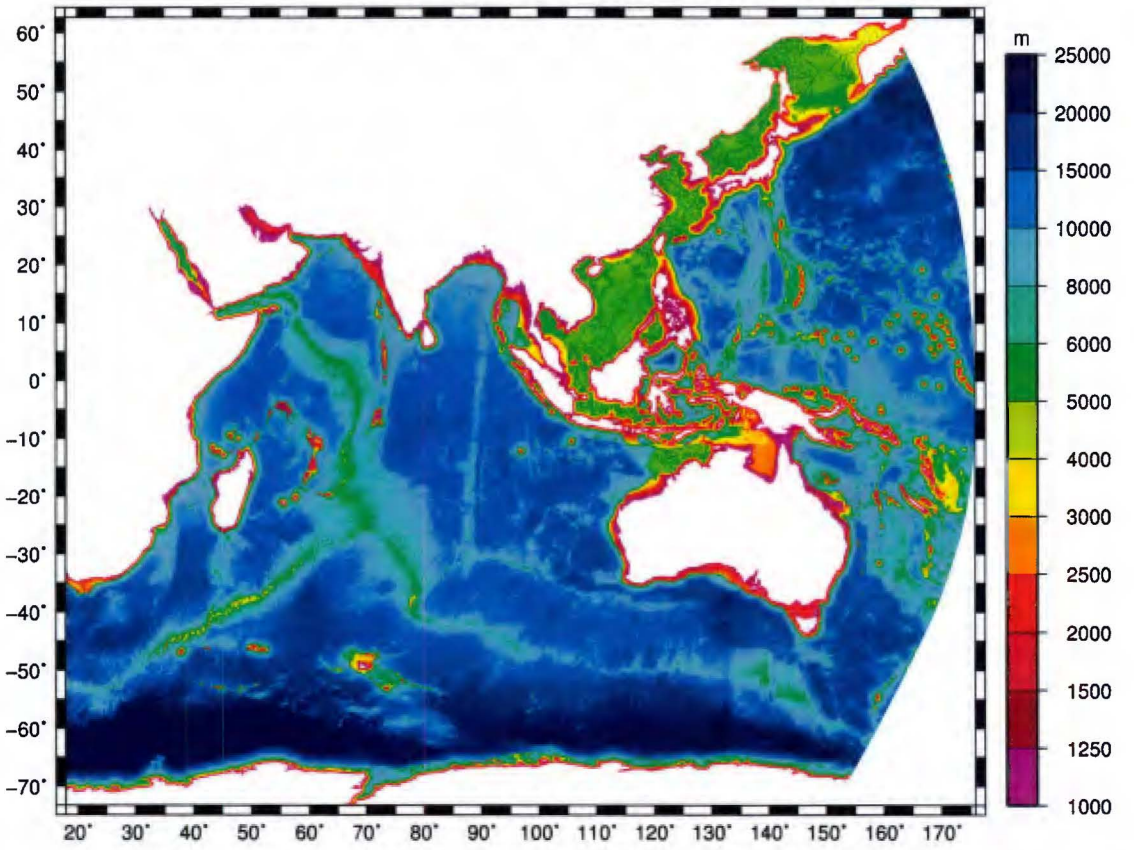

Figure 2: Resolution of the unstructured grid, which varies based on topographic gradients, depths and proximity to the coastline. The resolution at the coastline is ~1 km in most regions, and up to ~25 km in the deep and flat regions of the ocean.

on SRTM30_PLUS with newer measured nearshore bathymetry and topography sources thereby reducing the number of erroneous holes in the data. On top of this, 100 m Deepreef Explorer Great Barrier Reef and Coral Seas (GBR), and Kerguelen Plateau (KP) datasets were applied. It was discovered that Deepreef Explorer GBR in the Torres Strait/New Guinea Region matches substantially better with GEBCO_2014 than SRTM15_PLUS, thus GEBCO_2014 was applied locally here (differences between the two databases are discussed further in §5.2). Also, 90 m East Asia nearshore bathymetry datasets in the Philippines, Japan, Gulf of Thailand, South China Sea, and East China Sea regions; and local high-resolution bathymetry and grids privately obtained for Tokyo Bay and South Korea were applied. However, even in the high-resolution datasets, erroneous depth in harbor complexes and channels persist. These were corrected where possible using data from FUGAWI navigational charts (`https://www.fugawi.com/`). However, the errors in the final bathymetry that is applied to IndWPac are still largely uncertain.

3 ADCIRC Hydrodynamic Model

3.1 Governing Equations

The horizontal two-dimensional implementation of the Advanced Circulation coastal ocean model (ADCIRC-2DH) is used to calculate the hydrodynamics (Westerink et al., 2008; Westerink et al., 1992). The governing equations are the shallow water equations (SWE) in primitive, non-conservative, and barotropic form:

$$\frac{\partial \eta}{\partial t} + \nabla \cdot (\boldsymbol{u}H) + \sigma(\boldsymbol{x})(\eta - \eta_c) = 0 \tag{2}$$

$$\begin{aligned}\frac{\partial \boldsymbol{u}}{\partial t} + \boldsymbol{u} \cdot \nabla \boldsymbol{u} + f\mathbf{k} \times \boldsymbol{u} + g\nabla(\eta - \eta_{EQ} - \eta_{SAL}) + C_f \frac{|\boldsymbol{u}|\boldsymbol{u}}{H} + \mathbf{C}\boldsymbol{u} \\ - \frac{1}{H}\nabla \cdot [\nu_t H(\nabla \boldsymbol{u} + \nabla \boldsymbol{u}^{\mathrm{T}})] + \sigma(\boldsymbol{x})(\boldsymbol{u} - \boldsymbol{u_c}) = 0\end{aligned} \tag{3}$$

where η is the surface elevation, $H = h + \eta$ is the total water depth in which h is the still water depth, $\boldsymbol{u}$ is the depth-averaged velocity vector, g is the acceleration due to gravity, $\mathbf{k}$ is the vertical unit vector, and $f = 2\Omega \sin \phi$ is the Coriolis parameter in which Ω is the angular speed of the earth, and ϕ is the latitude. The quantity η_{EQ} is the equilibrium tide, and η_{SAL} is the ocean self-attraction and loading term (SAL). In the dissipation terms, C_f is the coefficient of bottom friction, $\mathbf{C}$ is the dissipation matrix due to the generation of internal tides, and ν_t is the horizontal eddy viscosity coefficient. Finally, we impose an absorption-generation sponge layer (e.g. Zhang et al., 2014) where, $\sigma(\boldsymbol{x})$ are the spatially varying absorption coefficients applied over the defined sponge boundary, and η_c and $\boldsymbol{u_c}$ are the corresponding reference solutions for surface elevation and velocity respectively.

3.2 Ocean Self-attraction and Loading Term

The ocean self-attracting and loading (SAL) term, η_{SAL} is related to the yielding of the solid Earth to tides and to the weight of the ocean and its self-attraction (Hendershott, 1972). For the large scale

Table 1: Bathymetric data sources, location applied, resolution and availability. Interpolation onto our grid is conducted in the order shown in this table

Name	Source(s)	Location	Resolution	Availability
SRTM30_PLUS	Becker et al. (2009)	globally >500 m depth	1/120°	free at website[1]
Abysall Hills	Goff and Arbic (2010) and Melet et al. (2013)	globally >500 m depth	1/120°	*prvt. comm.*
SRTM15_PLUS	Sandwell et al. (2014)	globally <500 m depth	1/240°	free at website[2]
TPXO8	Padman et al. (2002)	<65°S	1/30°	free at website[3]
GEBCO_2014	Weatherall et al. (2015)	Torres Strait/New Guinea	1/120°	free at website[4]
Deepreef Explorer GBR	Beaman (2010)	Great Barrier Reef & Coral Sea	1/1000°	free at website[5]
Deepreef Explorer KP	Beaman and O'Brien (2011)	Kerguelen Plateau	1/1000°	free at website[6]
TCarta Marine	TCarta Marine (2012)	East Asia nearshore	1/1200°	proprietary[7]
Tokyo Bay HR	Shintaro Bunya (*prvt. comm.*, 2015)	Tokyo Bay	FE grid	*prvt. comm.*
South Korea HR	SeungWon Suh (*prvt. comm.*, 2017)	South Korea	FE grid	*prvt. comm.*
Harbor hand-edits	FUGAWI Navigational Charts	various harbors and channels	FE grid	-

FE grid: indicates data was received on a finite-element grid
[1]: `ftp://topex.ucsd.edu/pub/srtm30_plus/`
[2]: `ftp://topex.ucsd.edu/pub/srtm15_plus/`
[3]: `http://volkov.oce.orst.edu/tides/tpxo8_atlas.html`
[4]: `http://www.gebco.net/data_and_products/gridded_bathymetry_data/`
[5]: `https://www.deepreef.org/bathymetry/65-3dgbr-bathy.html`
[6]: `https://www.deepreef.org/bathymetry/98-kergdem-bathy.html`
[7]: provided by Factory Mutual Insurance (FM Global), Norwood, MA

IndWPac domain it is essential to include the effect of SAL terms on the tides. However, since the model is regional, the global integrals of the tidal elevations required to be solved iteratively for the SAL terms (Ray, 1998) are not available. Thus, in this study the amplitudes and phases of SAL for each tidal constituent are simply interpolated from those used in the global data-assimilated model FES2014 (Lyard et al., 2006) onto our mesh and forced by reconstructing the time series from the constituents. Given the accuracy of state-of-the-art global data-assimilated models (Stammer et al., 2014), the slowly varying SAL terms obtained from these models are also assumed to be sufficiently accurate. However, the calculation of SAL through global integrals to obtain full consistency with the surface elevation (including non-periodic components) is ultimately desired (c.f. Apecechea et al., 2017).

3.3 Dissipation due to the Generation of Internal Tides

Internal tides generated by flow over rough bathymetry are major contributors to barotropic tidal energy dissipation in the deep ocean, equivalent to around 30% of the global total (Egbert and Ray, 2001). As a result, parameterization of this dissipation is necessary in barotropic numerical models that include expanses of ocean where major submarine ridges, island chains and shelf breaks that induce internal waves are present. In this study, parameterization of internal tide dissipation is particularly important since the Indian Ocean basin contains narrow shelves and vast expanses of open ocean where the dissipation due to internal tides over its well defined abyssal hills are crucial to the accuracy of the tidal solutions.

Parameterizations of internal tide dissipation are usually based on a linear wave drag type implementation valid only for subcritical topography ($\gamma < 1$). Here, $\gamma = \frac{||\nabla h||}{\alpha}$, in which $\alpha = \left(\frac{\omega^2 - f^2}{N_b^2 - \omega^2}\right)^{1/2}$ is the internal wave slope, ω is the angular frequency of the pertinent tidal wave (M_2 in this study), and N_b is the Brunt-Väisälä frequency at the seabed. In this study, we investigate two subcritical theory parameterizations for the dissipation matrix $\mathbf{C}$ in (3): one based only on local topographic features, and another that includes the nonlocal effects on wave generation.

First, we use a simple and robust parameterization that takes into account the directionality of dissipation (which we denote as the '*Directional*' method) similar to that presented by Lyard et al. (2006) is:

$$\mathbf{C} = C_{Dir} \frac{[(N_b^2 - \omega^2)(\tilde{N}^2 - \omega^2)]^{1/2}}{\omega} \begin{bmatrix} h_x^2 & h_x h_y \\ h_x h_y & h_y^2 \end{bmatrix} \tag{4}$$

where C_{Dir} is a scale factor, $\tilde{N}$ is the depth-averaged Brunt-Väisälä frequency, and the subscripts 'x' and 'y' indicate gradients in the longitudinal and latitudinal directions respectively. Note that we have substituted the typical wavenumber, κ in Lyard et al. (2006) for the fundamental internal mode at the pertinent tidal frequency (Zaron and Egbert, 2006). The *Directional* method only dissipates across slopes (rather than along them).

Second, a rigorous formulation for $\mathbf{C}$ that includes the nonlocal effects of the nearby topography on internal tide generation (Melet et al., 2013) was derived by Nycander (2005) (denoted as the '*Nycander*' method hereafter). It has the following form in a general coordinate system (Green and Nycander, 2013):

$$\mathbf{C} = C_{Nyc} \frac{N_b}{4\pi h} \sqrt{1 - \frac{f^2}{\omega^2}} \begin{bmatrix} 2J_x h_x^* & J_x h_y^* + J_y h_x^* \\ J_x h_y^* + J_y h_x^* & 2J_y h_y^* \end{bmatrix} \tag{5}$$

where C_{Nyc} is a scale factor, and J is a convolution integral of a filtered Green's function of the topographic heights h^* (defined positive from seabed) within a specified radius from the point of interest (c.f Green and Nycander, 2013; Nycander, 2005). Readers should refer to Green and

Nycander (2013) for the equations and numerical scheme to compute the gradients of J (J_x and J_y) on the structured grid of the bathymetric data.

The advantages of the *Directional* method is that $\mathbf{C}$ is positive definite, and it does not require the computationally intensive calculation of J allowing it to be quickly implemented into the model. On the other hand, the *Nycander* method allows for the nonlocal generation of internal tides. However, $\mathbf{C}$ in (5) is not guaranteed to be positive definite since the sign of the gradients of J and h^* do not necessarily conform. Furthermore, the calculation of the gradients of J are computationally expensive so it is not as readily implemented into a numerical model.

Note that for $h < 100$ m we set $\mathbf{C} = 0$ in both methods, because the topographic gradients on the continental shelf should be small, and bottom friction dissipation starts to dominate here.

Modifications to get a positive definite $\mathbf{C}$, and to incorporate the nonlocal effects of N_b into the *Nycander* method are implemented and briefly evaluated in this study. We also investigate whether the nonlocal wave generation effects captured by the *Nycander* method have a meaningful effect on the solution by comparing the results between the two methods (see §5.3).

3.4 Bottom Friction Dissipation

Dissipation due to bottom friction is known to account for a significant proportion of dissipation of the barotropic tides, particularly in shallow regions ($h \ll 100$ m). It is commonly assumed that the bottom stress is proportional to square of the depth-averaged velocity in barotropic tidal simulations (e.g. Buijsman et al., 2015; Green and David, 2013; Lyard et al., 2006) as adopted in (3). Values for the coefficient of bottom friction, C_f have been shown to range between orders 10^{-3} and 10^{-2} based on measurements in continental shelf and estuarine regions (e.g. You, 2005; Heathershaw, 1979; Heathershaw and Simpson, 1978; Charnock, 1959). Canonical global values of C_f equal to 2.5×10^{-3} (Lyard et al., 2006) or 3.0×10^{-3} (Egbert and Erofeeva, 2002) are usually applied as a spatial constant in large-scale tidal models.

It has been suggested that deviations from the canonical value of C_f globally do not significantly change the overall dissipation but that deviations by an order of ten can significantly degrade the tidal solution (Lyard et al., 2006). Nevertheless, if other dissipation mechanisms are reliable (internal tide) there is evidence that local variations in C_f over the range of physically plausible values (10^{-3} to 10^{-2}) can improve local tidal solutions (e.g Lefevre, Provost, and Lyard, 2000). In this study, we present a semi-data-informed method of calculating spatially varying C_f. The goal is not to obtain the 'optimal' C_f but merely to show that it is possible to calculate spatially varying C_f that locally improves tidal solutions based on some knowledge of the seabed and physical properties of the flow.

We start with the log-law formulation of C_f (Schlichting, 1979):

$$C_f = [\kappa / \ln(0.5H/z_0)]^2 \tag{6}$$

where $\kappa = 0.4$ is the von Kármán constant, and z_0 is the seabed roughness length which can be equated to an effective sediment roughness, k_s ($= 30z_0$). It is important to note that k_s is not simply a function of the sediment roughness (grain-size) itself, rather it is mainly determined by the heights of ripples and dunes (bedforms) that form due to the prevailing currents which can be a major source of the resultant bed stress (Heathershaw, 1979). To estimate k_s that takes into account the bedform heights, we use empirical equations (Rijn, 2007) that are a function of median sediment grain diameter d_{50}, sediment density relative to water s, an effective mean current speed u_f, and the depth h (see A). The empirical equations return small values of k_s when either the sediments are light and the tidal currents are strong flattening out the bed, or when the sediment grains are too heavy for the currents to create bedforms. In between these extremes, ripples and dunes will form resulting in larger values of k_s.

To obtain the sediment grain sizes we make use of a database of the census of the world's seafloor sediment types (Dutkiewicz et al., 2015). We map these sediment types onto physically reasonable values of d_{50} (see Table 2). For pelagic type sediments (oozes and clays) C_f is set to 2.5×10^{-3} as a default roughness. Relative sediment density $s = 1.722$ (dry bulk density by mass of sand, Rijn, 2007) for $d_{50} \geq d_{sand}$, $s = 1.2$ (natural sediment with organic materials involved, Rijn, 2007) for $d_{50} \leq d_{silt}$, and is linearly interpolated in between. Here, $d_{sand} = 6.2\times10^{-5}$ m, and $d_{silt} = 3.2\times10^{-5}$ m, where the assumption is made that the finer-sized sediments in the census database contain a higher percentage of lighter organic material. The effective mean current speed u_f is defined as (Zaron, 2017):

$$u_f = \left(u_0^2 + 0.5 \sum_k |\boldsymbol{U}^k|^2 \right)^{0.5} \tag{7}$$

where u_0 is a constant non-tidal current (Snyder, Sidjabat, and Filloux, 1979), that we set equal to 0.25 m/s (Zaron, 2017), and $\boldsymbol{U}^k$ (both x and y components) is the amplitude of the k^{th} tidal current constituent. The spatially constant $C_f = 2.5\times10^{-3}$ simulation is used to approximate u_f in order to compute the spatially varying C_f map (Fig. 3).

3.5 Lateral Eddy Viscosity

To include lateral eddy viscosity in ADCIRC, the Smagorinsky model (Smagorinsky, 1963) is used to evaluate ν_t since it changes with the local mean strain-rate providing a degree of physical fidelity, as well as providing stability to the advection terms. ν_t is calculated as follows (Dresback, Kolar, and Luettich, Jr., 2005):

$$\nu_t = C_\mu A_E \sqrt{(\nabla \cdot \boldsymbol{u}^T)^2 + (\nabla \times \boldsymbol{u}^T)^2} \tag{8}$$

where C_μ is a free coefficient that we set equal to 0.2, and A_E is the local element area.

3.6 Lateral Boundary Conditions

Lateral open ocean boundaries are forced by reconstructing the elevations from the tidal constituents obtained from a global data-assimilative model, TPXO8 (Egbert and Erofeeva, 2002). In this study we force with the major semi-diurnal (M_2, N_2, S_2, K_2) and diurnal (K_1, O_1, P_1, Q_1) constituents, which are also used to force the SAL and equilibrium potential terms. Prescribing the elevations at the open boundaries is a reflecting boundary condition that allows the velocities to freely satisfy the governing equations. In some cases this condition can generate spurious modes that may lead to instabilities. Utilizing an absorption-generation sponge layer can reduce the production of these modes, as demonstrated in §5.1.

Table 2: Median grain sizes d_{50} and relative density s for each sediment type used in the calculation of C_f

Sediment Type	d_{50} [m]	s
Gravel and coarser	3.0×10^{-3}	1.722
Sand	1.0×10^{-4}	1.722
Silt	5.0×10^{-5}	1.513
Ash and volcanic sand/gravel	1.0×10^{-3}	1.722
Siliceous mud	4.0×10^{-5}	1.339
Fine-grained calcareous sediment	4.5×10^{-5}	1.426

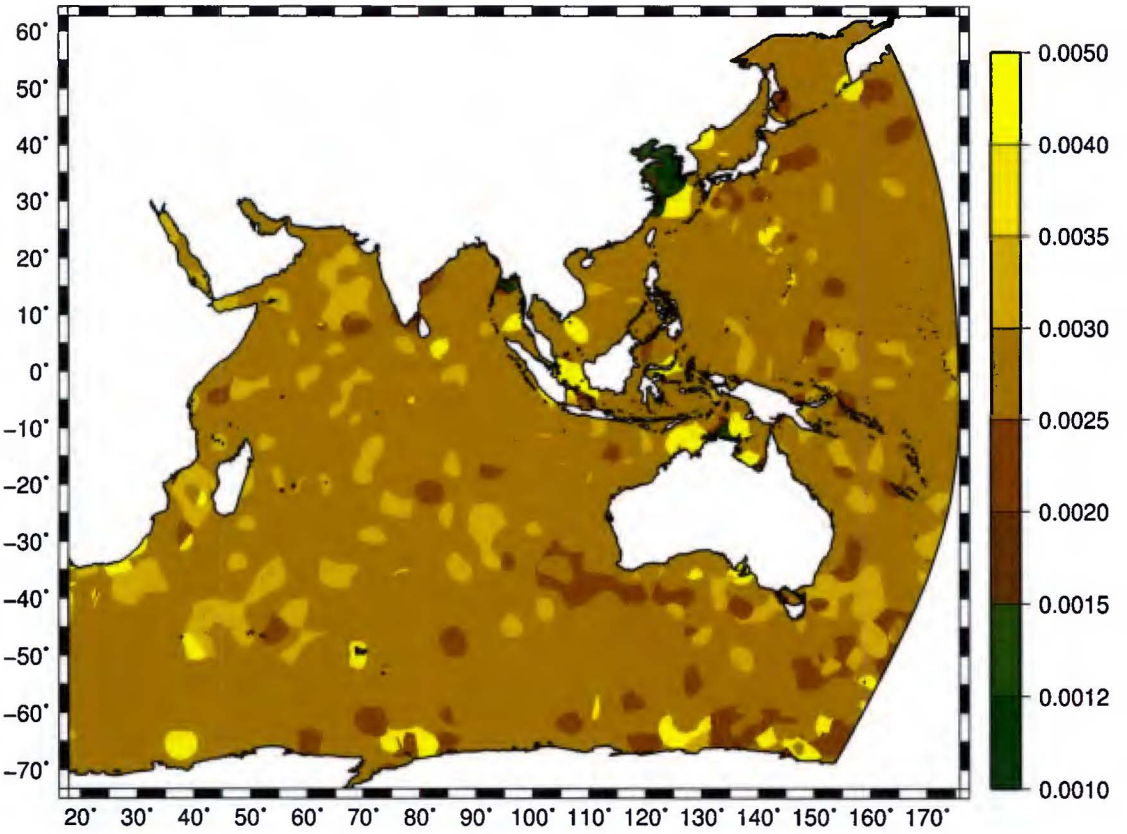

Figure 3: Map of bottom friction coefficients C_f based on sediment types (Dutkiewicz et al., 2015) with assumed grain size and sediment density (Table 2). The empirical equations (Rijn, 2007) also take into account depth and tidal velocities.

Firstly, the location and width of the sponge layer l must be specified. We take l to be approximately equal to 10% the length of the M_2 tidal wave, λ_{M_2}. The overall solution was found to be fairly insensitive to the choice of sponge layer width, but for $l < 0.1\lambda_{M_2}$ the solutions may not match well across the sponge-calculation domain interface. To show the location and width of the sponge layer region, a hatched '+' region is included in figures throughout this paper.

In addition, the sponge layer requires spatially varying absorption coefficients $\sigma(\boldsymbol{x})$, and reference solutions of the free surface η_c and velocities $\boldsymbol{u}_c$. Assuming a polynomial type function for the absorptive coefficients inside the sponge layer, they are derived from the linear shallow water solution:

$$\sigma = \sigma_m \left(\frac{r}{l}\right)^{\alpha} \tag{9}$$

$$\sigma_m = -\frac{\sqrt{gh}(\alpha+1)\ln(1/F)}{l(r_c/l)^{\alpha+1}} \tag{10}$$

where r is the distance from the edge of the sponge layer, α is the order of the polynomial function, F is the reduction factor of the outgoing wave at the position r_c from the edge of the sponge. The

parameters $\alpha = 2$, $F = 20$ and $r_c/l = 0.5$ are chosen in this study but the solution is not typically sensitive to the choice of these factors. The reference solutions are interpolated from TPXO8 tidal constituents in the same way we specify the lateral boundary. Note that to get $\boldsymbol{u}_c$, the conservative transport variable ($\boldsymbol{u}_c h$) is interpolated from TPXO8 before dividing this by the nodal depths on our grid for additional consistency.

3.7 Finite-Element Solution

ADCIRC solves the governing equations in a continuous-Galerkin framework, where the generalized wave continuity equation (GWCE) is utilized to eliminate spurious modes (c.f. Westerink et al., 1992). The two-part symmetrical velocity based method for the lateral stress terms (Dresback, Kolar, and Luettich, Jr., 2005), and explicit mass-lumping mode are used to solve the GWCE in this study.

A time step $\Delta t = 2$ s can be used with our current grid without generating Courant-Friedrichs-Lewy (CFL) induced numerical instabilities. Wall-clock times are approximately 11 min day^{-1} of simulation time using 960 computational cores ($\approx 10,000$ finite-element nodes per core) of a high-performance computing machine with Haswell processors and a Mellanox FDR Infiniband network connection. To validate the model with observations, we simulated for 195 days, including a 15 day spin-up from a completely zero state. The final 180 days are used for the harmonic analysis of the tides. The long six month time period is required to correctly separate all the tidal constituents of interest (e.g K_1 and P_1).

4 Summary of Tidal Validation from Best Model Setup

4.1 Best Model Setup

To obtain the best model setup we first found the global amplification factor of the internal tide dissipation parameter so that the model skill versus TPXO8 was maximized in the deep ocean ($h > 500$ m). A positive definite and spatially smoothed N_b modified version of the *Nycander* method with $C_{Nyc} = 2.9$ and local multiplier coefficients over the Luzon Strait (see §5.3) was decided on. Local bathymetry datasets and hand-edits were applied to shallow water regions and responses against coastal tide gauges were checked for reliability in the harmonic analysis. Finally, a map of varying bottom friction dissipation coefficients C_f was calculated based on some information of the local sediment types, as described in §3.4, in an attempt to increase the model skill versus using a spatially constant C_f. The best model setup is denoted by '*Comp + IT + SV*', indicating the use of our *comprehensive* bathymetric data (Table 1), optimal *internal tide* dissipation, and *spatially varying* C_f.

4.2 Measure of Model Skill

To measure the skill of the model for the purpose of determining and evaluating the best setup, we compare with the root-mean-square (RMS) discrepancy D of the elevation (either for a single tidal constituent or for the total free surface) at a point. D is the average of the squared differences between measured and observed elevations integrated over a long period of time. It is calculated in this study using the sum of the vector differences of the in-phase ($A^k \cos\theta^k$) and quadrature

$(A^k \sin\theta^k)$ components of each constituent (Wang et al., 2012):

$$D = \left(0.5 \sum_k \left[(A_0^k)^2 + (A_m^k)^2 - 2A_0^k A_m^k \cos(\theta_0^k - \theta_m^k) \right] \right)^{1/2} \tag{11}$$

where A^k and θ^k are the amplitudes and phase lags of the k^{th} constituent respectively, and the subscripts 'o' and 'm' refer to the observed and modeled values respectively. In addition, the relative RMS discrepancy $RD = D/V$, where V is the absolute average value of the variability in the free surface elevation, and is calculated by (Wang et al., 2012):

$$V = \left[0.5 \sum_k (A_0^k)^2 \right]^{1/2} \tag{12}$$

For an overview of the spatial distribution, we include scatter plots of D and RD at the tide gauges (and contour plots versus TPXO8) in order to highlight regions of notably small or large discrepancies. However, to obtain a single global metric of performance the mean of the discrepancy D, denoted $\overline{D}$, or the mean of RD, denoted $\overline{RD}$, is used. Note that when calculating $\overline{D}$ over a region to compare against TPXO8 (tpx) this is computed as:

$$\overline{D}_{tpx} = \frac{\iint D \, dA}{\iint dA} \tag{13}$$

where $\iint dA$ indicates an area integral that is performed over the elements of the grid. When comparing against tide gauges ($\overline{D}_{tg}$, $\overline{RD}_{tg}$), the arithmetic average is used. In comparison to $\overline{D}$, the RMSE metric commonly used (e.g Stammer et al., 2014; Buijsman et al., 2015) is:

$$\text{RMSE} = \sqrt{\frac{\iint D^2 \, dA}{\iint dA}} \tag{14}$$

i.e. it is the square-root of the mean of D^2 and is always larger than $\overline{D}$. The RMSE may experience abrupt changes with depth and tends to overestimate the overall discrepancy (Wang et al., 2012). In contrast, $\overline{D}$ has been shown to decrease monotonically with depth (Wang et al., 2012), thus we chose to predominantly use $\overline{D}$. However, we also quote values of RMSE for comparison with those reported in other studies.

4.3 Tidal Gauge Database

A database of harmonic constituents consisting of 39 deep-water stations, 62 shallow water/shelf stations, and 659 unique coastal tide gauge locations was assembled from multiple sources for the computational domain (detailed in Table 3). Within the *coastal* tide gauge set there are a number of data-points duplicated between sources so we set up a hierarchy between the different sources to decide what value to use in our model evaluation based on perceived reliability (Table 3 is listed in hierarchical order, and the number of stations listed for each source is the eventual number after removal of duplicates).

The KHOA (Korean Hydrographic and Oceanographic Agency), GESLA-2 (Global Extreme Sea Level Analysis), and UHSLC FD (University of Hawaii Sea Level Center *fast-delivery*) databases contain long-term hourly time series of elevations. We have used the Utide MATLAB function

ut_solv (Codiga, 2011), which uses the iteratively-weighted least-square harmonic analysis technique, to obtain up to 68 tidal constituents. Within some of the sources, not all of the main eight constituents are necessarily posted such as in the JMA, NBoB, SCS, Yellow Sea, most of IHO, and TOPEX/POSEIDON Crossover sets (M_2, S_2, K_1, O_1 only). The Java Sea/SCS set excludes K_2 and P_1. The ST727 excludes various constituents (often just Q_1) at approximately half of the locations. Occasionally, locations in the GESLA_2, and Truth_Shallow sets miss one or two of the eight main constituents due to short analyses. Additionally, posted geographical locations are often to the nearest $1'$ or $0.1'$, so we have checked station positions to ensure that they are likely to be in the correct location, in particular not on land. The FUGAWI navigational charts often indicate known locations of tide gauges and were used to correct locations where applicable. Some stations were excluded because they were located just outside of our computational grid (in back-bays, rivers, etc.). The locations and constituent values used to conduct the statistical comparisons in this study (sans proprietary data) can be found at Pringle (2017).

A detailed discussion on the harmonic analyses and uncertainties of the tidal constituents (extended globally) will be reported in a subsequent paper. For example, the constituents from the IHO and ST727 gauges are derived between 1848-1970 and may have larger error margins. In addition, the rate at which the coasts are changing globally is accelerating, and elimination of wetlands, land reclamation, and deep dredging of channels and ports may impact tidal constituents which are typically located within harbor complexes in support of navigation.

4.4 Overall Global Assessment

We start by showing the global responses of the M_2 and K_1 (Fig 4) tidal waves, and their RMS discrepancies against TPXO8 (D_{tpx}) for the $Comp + IT + SV$ model setup. The general response is well described for both constituents by our model including positions of most amphidromes. Obvious exceptions are the M_2 amphidromes off the south-west tip of Australia and near Mawson Station, Antarctica. The positions of these amphidromes and the solution in the Southern Ocean were found

Table 3: Tide gauge data sources, number and availability. Listed in hierarchical order for the *coastal* gauges

Name	Source	Number	Type	Availability
Truth_Pelagic	Shum et al. (1997)	31	deep-water const.	free at website[1]
Truth_Shallow	Stammer et al. (2014)	52	shallow-water const.	free at website[1]
TOPEX/POSEIDON Crossovers	Robertson and Ffield (2008)	8/5	deep/shallow-water const.	listed in paper
Java Sea/SCS	Wei et al. (2016)	5	shallow-water const.	listed in paper
NOAA	NOAA Tides and Currents (2017)	4	coastal const.	free at website[2]
JMA	Japanese Meteorological Agency (2017)	181	coastal const.	free at website[3]
AusTides	Australian National Tide Tables (2013)	63	coastal const.	proprietary
KHOA	Korean Hydrographic and Oceanographic Agency (2017)	35	coastal elev.	free at website[4]
GESLA-2	Woodworth et al. (2017)	107	coastal elev.	free at website[5]
UHSLC FD	Caldwell, Merrifield, and Thompson (2015)	19	coastal elev.	free at website[6]
NBoB	Krien et al., 2016	2	coastal const.	listed in paper
SCS	Fang et al. (1999)	29	coastal const.	listed in paper
Yellow Sea	Fang et al. (2004)	6	coastal const.	listed in paper
ST727	British Hydrographic Institute (c.1848-1970)	130	coastal const.	free at website[1]
IHO	International Hydrographic Office (1990)	83	coastal const.	proprietary

const.: indicates data is available directly as harmonic constituents
elev.: indicates data is available as time series of elevations
[1]: `ftp://ftp.legos.obs-mip.fr/pub/FES2012-project/data/gauges/2013-12-16/`
[2]: `https://tidesandcurrents.noaa.gov/gmap3/`
[3]: `http://www.data.jma.go.jp/kaiyou/db/tide/suisan/station2017.php`
[4]: `http://www.khoa.go.kr/koofs/kor/observation/obs_real.do`
[5]: `http://www.gesla.org/`
[6]: `ftp://ftp.soest.hawaii.edu/uhslc/fast`

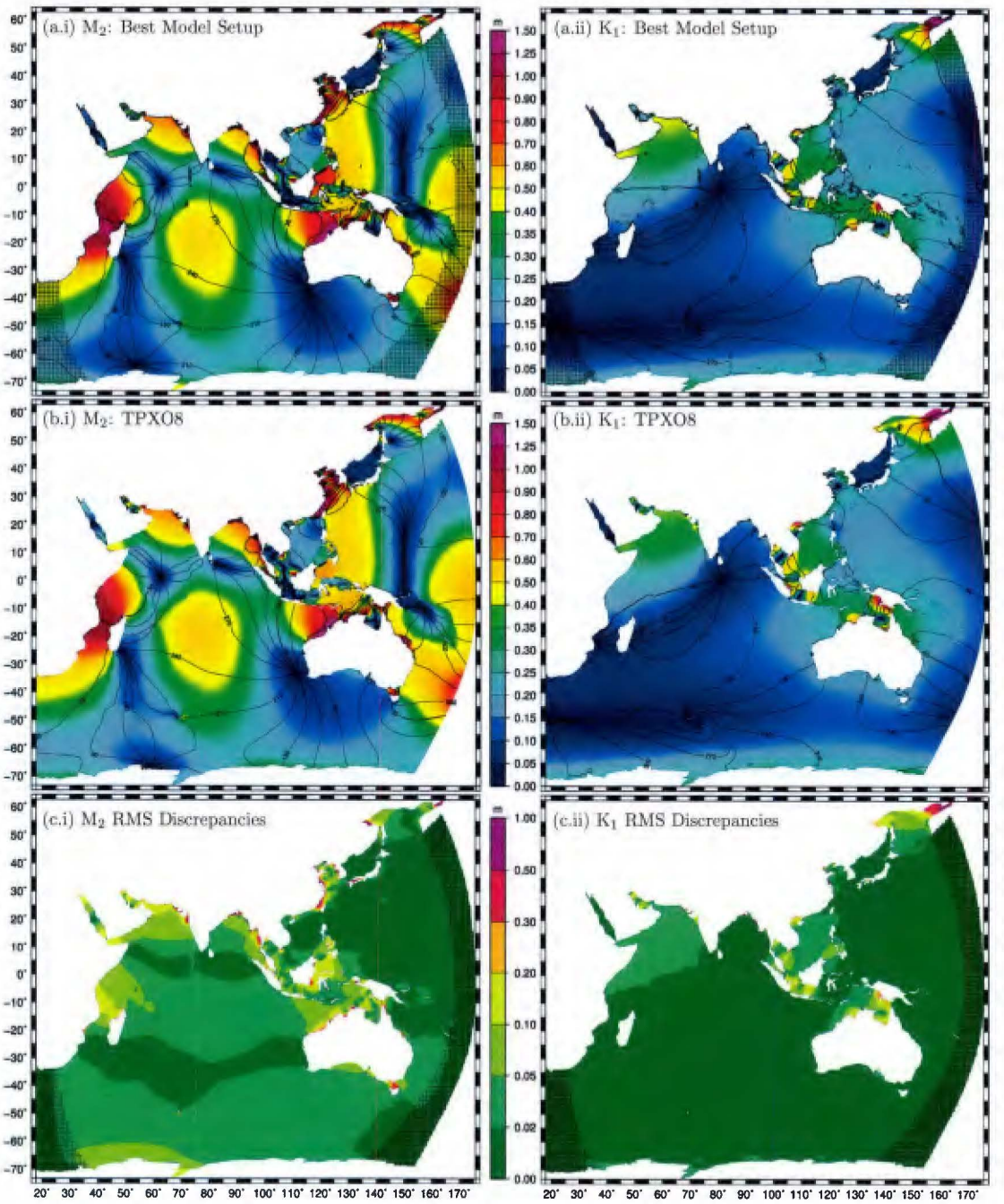

Figure 4: Amplitude (m) and phase responses of the (i) M_2 and (ii) K_1 tidal waves; (a) *Comp + IT + SV* model setup, (b) TPXO8 model (obtained from `http://volkov.oce.orst.edu/tides/tpxo8_atlas.html`), (c) RMS discrepancies (m) between *Comp + IT+ SV* model setup and TPXO8, D_{tpx}. '+' hatched regions indicate absorptive sponge zone.

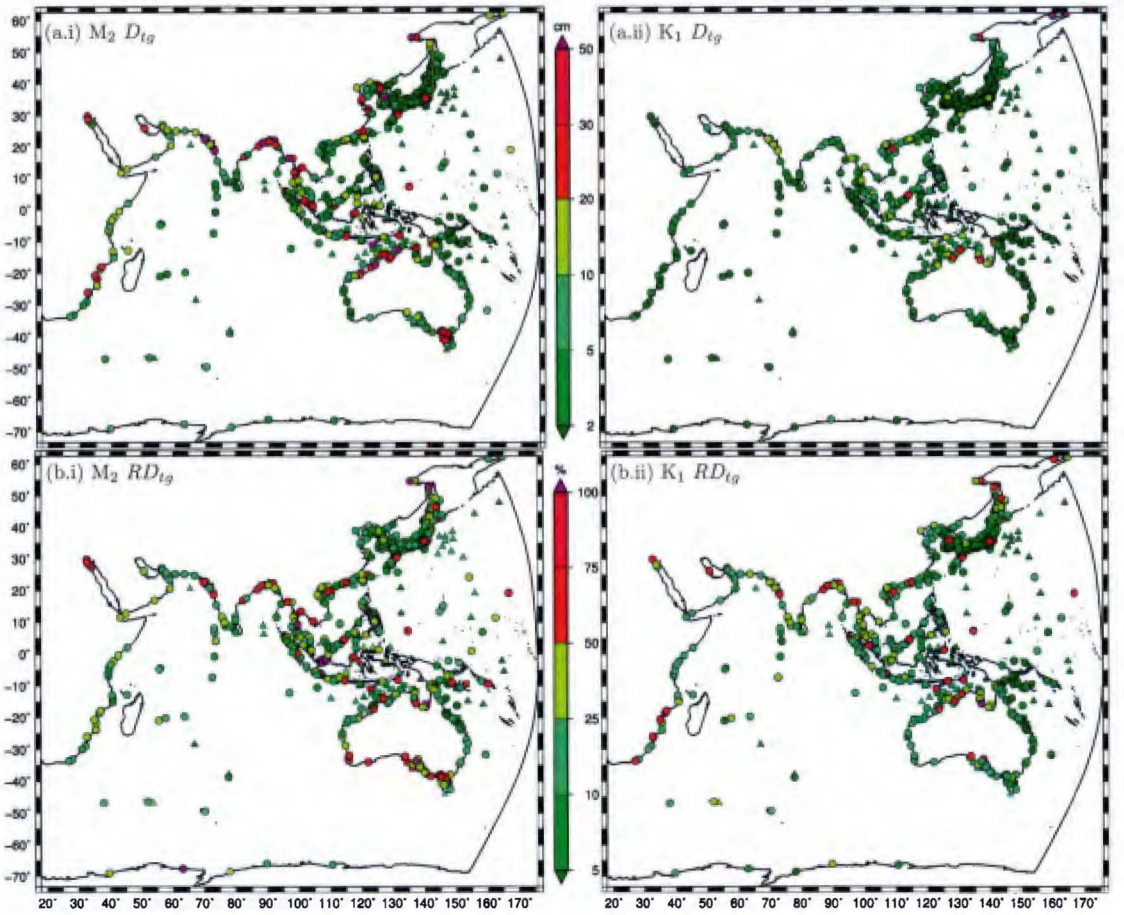

Figure 5: Spatial distribution of discrepancies of the (i) M_2 and (ii) K_1 tidal waves versus tide gauges for the *Comp + IT + SV* model setup; (a) RMS discrepancy D_{tg}, (b) relative RMS discrepancy RD_{tg}. Triangles: deep water gauges, Squares: continental shelf water gauges, Circles: coastal tide gauges.

to be very sensitive to the boundary conditions applied in this study and may be impacted by the TPXO8 derived velocities in the absorption-generation sponge layer (see §5.1).

The spatial distribution of the RMS discrepancies (D_{tg}) and relative discrepancies (RD_{tg}) for the *Comp + IT + SV* model setup against tide gauges are also illustrated (Fig 5). Overall, tide gauges with similar discrepancies are generally clustered together, and there is a relatively strong spatial correlation between discrepancies against TPXO8 and those at tide gauges. Exceptions to this include much of the inner coast of the Yellow Sea and the Seto Inland Sea where the TPXO8 model may not be reliable. The *Comp + IT + SV* model setup performs particularly well throughout the western Pacific Ocean including along the Japanese archipelago and northeastern Australia for both constituents. Notable wide-spread RMS discrepancies in the M_2 tidal wave appear in the Mozambique Channel, north and west Arabian Sea, Red Sea, Sea of Okhotsk, Andaman Sea, Yellow Sea, northern Australian shelf and the Celebes Sea. K_1 RMS discrepancies are notable in the Sea

of Okhotsk, Arabian Sea, South China Sea and Java Seas, and the Arafura Sea. Predominantly large tidal ranges account for the discrepancies shown. For example, M_2 RD_{tg} values are relatively small in the Yellow Sea even though D_{tpx} values appear large in the Yellow Sea for the *Comp + IT + SV* model setup. In fact, the response is improved rather substantially from the *Comp + IT + SC* model setup here (§5.4). RD_{tg} is also less significant than D_{tg} in the Mozambique Channel and northern Australian shelf. These two regions are heavily influenced by large-scale effects related to lateral boundary conditions (§5.1) and internal tide dissipation (§5.3).

On the other hand, both D_{tg} and RD_{tg} are large in the Sea of Okhotsk for both constituents. The importance of bathymetry in the region (which is not well known) has been highlighted by Zaron (2017). The Celebes Sea is also a problem area for M_2 that is most likely a result of incorrect flux exchanges through the island chains due to inadequate bathymetry and a poor representation of internal tide dissipation particularly in shallow waters. It should be noted that the Celebes Sea and surrounding Indonesian seas was a focus of the original TPXO study (Egbert and Erofeeva, 2002) due to its poor forward model responses, and the region has been found to cause problems for three-dimensional ocean circulation models (Robertson and Ffield, 2008; Ngodock et al., 2016). The South China and Java Sea region extending down to the Torres Strait has a relatively large diurnal tidal range and K_1 D_{tg} and RD_{tg} values are not small compared to most of the domain. The physics of the K_1 tidal wave here can be thought of as a standing wave where the response is likely to depend highly on the overall bathymetry and shoreline of the region. The region is also

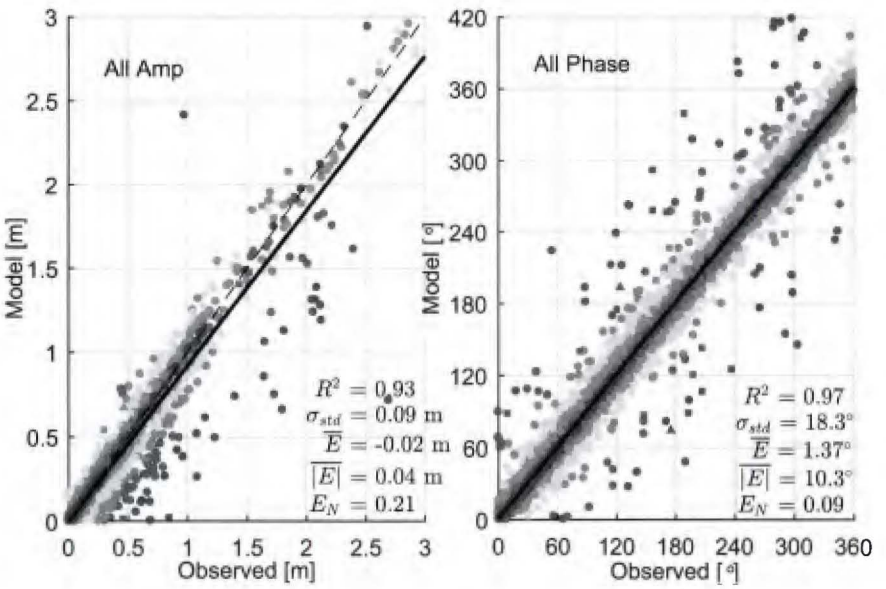

Figure 6: Amplitudes, A (left) and phase lags, θ (right) of up to all eight major tidal constituents for the *Comp + IT + SV* model setup versus observed values at tide gauges. Triangles: deep water gauges, Squares: continental shelf water gauges, Circles: coastal tide gauges. Colors of markers for the amplitude refer to the absolute error (m) between model and observed. Colors of markers for the phase refer to the absolute errors normalized by 180° between model and observed. The same color scale as Fig 5(a) is used for both. Statistics shown on the figure are as follows: R^2 is the coefficient of determination, σ_{std} is the standard deviation of the error, $\overline{E}$ is the mean error, $\overline{|E|}$ is the mean absolute error, and E_N is the normalized mean absolute error.

heavily influenced by the energy flux permitted through the Luzon Strait which is largely controlled by internal tide dissipation (§5.3). Note that in some areas such as between South China Sea and Java Sea, which has a small M_2 tidal range because it is close to an amphidrome, RD_{tg} becomes very large however D_{tg} is relatively small.

A summary of the global tide gauge errors shown in terms of amplitudes ($R^2 = 0.93$, $\sigma_{std} = 0.09$ m, $\overline{|E|} = 0.04$ m) and phases ($R^2 = 0.97$, $\sigma_{std} = 18.3°$, $\overline{|E|} = 10.3°$) of up to all eight major tidal constituents from the *Comp + IT + SV* model setup against the observed values is presented (Fig 6, see caption for definitions of error metrics). There are a total of 6080 data points on each plot. Just 2.4% of them represent absolute amplitude errors > 0.2 m, and 2.9% represent absolute phase errors > 36° (colored orange to purple in Fig 6). Outliers in the amplitudes of constituents tend to be underestimates rather than overestimates which may indicate deltaic regions, estuaries, back-bays and rivers where the bathymetry is inadequate and overly dissipative, e.g. the Ganges Delta where large discrepancies are present (Fig 5). Aside from these regions, there is a consistent spread of errors for both the amplitudes ($\overline{E}$ = -0.02 m) and phases ($\overline{E} = 1.37°$) indicating a largely unbiased system.

4.5 Assessment in Deep, Shelf, and Coastal Waters

This section summarizes the results by dividing them into regions based on depth and proximity to the coastline. The three regions are as follows: deep water ($h > 500$ m), continental shelf and slope waters ($25 < h < 500$ m), and coastal waters (includes continental and island coastlines). Table 4 compares discrepancies between the various IndWPac model setups (different bathymetry datasets, with and without internal tide dissipation and spatially varying bottom friction coefficients), at the tide gauges and the TPXO8 atlas for these three regions. Note that when the interpolation of TPXO8 to the coastal tide gauges was performed using their native data extraction program OTPS2, a total of 93 locations returned a null value. Thus, for a fair comparison we present our model results against this reduced set of stations. The statistics of the IndWPac model were not noticeably different for the full coastal gauge set.

4.5.1 Discrepancy in Deep Water

The total free surface mean discrepancies for the *Comp + IT + SV* model setup ($\overline{D}_{tg} = 4.7$ cm, $\overline{RD}_{tg} = 13\%$) are 2.4 times those of the TPXO8 atlas ($\overline{D}_{tg} = 2.0$ cm, $\overline{RD}_{tg} = 5.5\%$) at the deep water tide gauges. The IndWPac model discrepancies in deep water are predominantly affected by the internal tide dissipation which reduces the total free surface RMS discrepancy by 47% ($\overline{D}_{tpx}$) and 55% ($\overline{D}_{tg}$). Different bathymetry datasets and bottom friction coefficients have little effect. Hotspots of discrepancy against deep water tide gauges for the IndWPac model occur in the Celebes Sea and Banda Sea (see Fig 5) against TOPEX/POSEIDON satellite crossover observations (Robertson and Ffield, 2008), particularly for the M_2 tidal wave. Without the crossover points (which are technically not tide gauges) the M_2 $\overline{D}_{tg}$ for the *Comp + IT + SV* model setup is closer to 2 cm instead of 3.6 cm.

A non-assimilative hydrodynamic model (Buijsman et al., 2015) achieves an RMSE of approximately 4 cm in the Indian and Pacific Oceans, and most hydrodynamics models give an RMSE greater than 5 cm (Stammer et al., 2014) globally for the M_2 tidal wave in waters deeper than 1000 m against TPXO8. In comparison, the *Comp + IT + SV* model setup gives RMSE = 3.6 cm. While the discrepancy for our model is somewhat smaller than other hydrodynamic models, it is not a significant change despite generally higher resolution of the grid and nearshore bathymetric data. As shown, only internal tide dissipation resulted in a notable reduction to the deep water discrepan-

Table 4: The mean RMS ($\overline{D}_{tg}$) and relative RMS ($\overline{RD}_{tg}$) discrepancies of the M_2, K_1, and the total free surface (up to all eight major constituents combined) at tide gauges for various IndWPac model setups plus the TPXO8 atlas (`http://volkov.oce.orst.edu/tides/tpxo8_atlas.html`), separated into three different regions (deep, continental shelf and slope, and coastal). The mean RMS discrepancy against TPXO8 ($\overline{D}_{tpx}$) is shown in deep, and continental shelf and slope waters. Stations numbers, units, and standard deviations are in parentheses

			Model					
Region	Error Metric	Tidal Wave	*Comp + NoIT + SC*	*GEBCO + IT + SC*	*SRTM + IT + SC*	*Comp + IT + SC*	*Comp + IT + SV*	TPXO8
Deep (39)	$\overline{D}_{tpx}$ (cm)	M_2	5.69 (4.31)	2.97 (2.21)	2.92 (2.26)	2.90 (2.20)	2.89 (2.18)	-
		K_1	1.39 (1.56)	1.08 (3.14)	1.01 (3.59)	0.95 (1.19)	0.95 (1.17)	-
		All	6.91 (4.76)	3.85 (5.51)	3.82 (6.23)	3.67 (2.59)	3.67 (2.56)	-
	$\overline{D}_{tg}$ (cm)	M_2	8.90 (9.97)	3.90 (4.40)	3.82 (4.02)	3.66 (4.45)	3.55 (4.34)	0.86 (0.87)
		K_1	2.16 (1.66)	1.03 (0.82)	0.94 (0.71)	0.93 (0.71)	0.92 (0.68)	0.50 (0.34)
		All	10.8 (11.0)	5.09 (5.03)	5.02 (4.60)	4.82 (4.98)	4.71 (4.89)	2.02 (2.82)
	$\overline{RD}_{tg}$ (%)	M_2	32.7 (25.7)	15.7 (11.4)	15.7 (11.3)	14.2 (11.9)	13.9 (11.7)	3.82 (3.31)
		K_1	16.4 (9.08)	8.40 (6.31)	7.72 (5.72)	7.67 (5.84)	7.69 (5.83)	4.29 (3.34)
		All	28.4 (19.8)	14.3 (10.2)	14.3 (9.35)	13.4 (10.3)	13.1 (10.1)	5.46 (5.67)
Shelf (62)	$\overline{D}_{tpx}$ (cm)	M_2	11.2 (11.0)	8.05 (9.02)	7.58 (9.45)	6.76 (7.67)	6.48 (7.76)	-
		K_1	5.83 (13.7)	6.69 (14.4)	6.57 (17.2)	4.52 (7.08)	4.75 (7.71)	-
		All	16.6 (22.1)	15.0 (23.6)	14.8 (28.7)	10.9 (10.8)	11.0 (11.4)	-
	$\overline{D}_{tg}$ (cm)	M_2	18.4 (12.1)	12.3 (11.4)	14.9 (19.3)	9.70 (9.63)	9.35 (9.87)	2.91 (3.28)
		K_1	5.71 (4.54)	4.41 (4.05)	4.84 (5.04)	3.71 (4.13)	4.47 (4.78)	1.60 (1.56)
		All	22.8 (12.3)	16.0 (11.7)	19.4 (20.8)	13.0 (11.0)	13.4 (11.4)	5.41 (3.76)
	$\overline{RD}_{tg}$ (%)	M_2	76.9 (89.1)	53.8 (73.3)	52.6 (65.4)	42.1 (58.5)	40.9 (55.8)	12.8 (20.9)
		K_1	24.4 (14.5)	21.0 (18.9)	21.5 (20.0)	19.0 (20.0)	19.9 (20.0)	7.89 (9.37)
		All	40.2 (18.1)	26.8 (15.0)	29.9 (19.8)	22.1 (14.8)	22.6 (16.1)	9.24 (5.37)
Coast (659)	$\overline{D}_{tg}$ (cm)	M_2	16.0 (17.1)	24.6 (33.4)	17.9 (24.1)	12.1 (15.6)	10.5 (14.4)	13.5 (39.3)
		K_1	4.58 (6.15)	6.95 (9.18)	5.45 (7.80)	4.09 (6.34)	3.90 (6.32)	3.12 (5.58)
		All	20.9 (19.6)	29.9 (37.1)	22.5 (27.4)	15.8 (18.4)	14.4 (17.2)	17.0 (47.9)
	$\overline{RD}_{tg}$ (%)	M_2	45.9 (60.4)	45.7 (44.0)	36.3 (40.1)	28.5 (36.9)	27.2 (38.4)	24.7 (38.6)
		K_1	27.0 (38.2)	37.9 (33.8)	29.0 (27.4)	22.4 (19.9)	21.6 (20.5)	18.1 (21.4)
		All	36.4 (22.5)	41.6 (31.9)	32.8 (26.0)	25.3 (18.2)	24.4 (19.2)	22.8 (30.8)

Model Setups
Bathymetry: '*GEBCO*' uses GEBCO_2014 bathymetric data, '*SRTM*' uses SRTM15_PLUS bathymetric data, '*Comp*' uses our comprehensive bathymetric data (Table 1)
Internal Tide Dissipation: '*NoIT*' does not include internal tide dissipation, '*IT*' uses the optimal internal tide parameters
Bottom Friction: '*SC*' uses a spatially constant $C_f = 2.5\times10^{-3}$, '*SV*' uses the spatially varying C_f map (Fig.3)

cies. Better nearshore bathymetry and grid resolutions do not allow for significant improvements in the internal tide dissipation matrix compared with coarser grid models because its calculation relies mostly on the deep water satellite altimetry data in global bathymetric datasets that is still limited to $>$ 10 km resolution accuracy (Goff and Arbic, 2010). Furthermore, the topographic roughness can be calculated on the relatively fine $\sim$1 km bathymetric grid before being interpolated onto the coarser computational grid for parameterization in barotropic models, reducing the requirement for a fine grid in the ocean.

4.5.2 Discrepancy in Continental Shelf and Slope Waters

The total free surface $\overline{D}_{tg}$ at tide gauges on the continental shelf are 2.6 to 2.8 times larger than those in deep water for both the *Comp + IT + SV* model setup and the TPXO8 atlas. Similar to deep water regions, the *Comp + IT + SV* model total free surface discrepancies ($\overline{D}_{tg}$ = 13 cm, $\overline{RD}_{tg}$ = 23%) are 2.5 times those of the TPXO8 atlas ($\overline{D}_{tg}$ = 5.4 cm, $\overline{RD}_{tg}$ = 9.2%) at the tide gauges on the continental shelf. The most significant factors in reducing the total free surface discrepancies are internal tide (34% reduction in $\overline{D}_{tpx}$) and the nearshore bathymetric datasets (26% reduction in $\overline{D}_{tpx}$). The bottom friction coefficient has a small impact overall, although the discrepancy for the K_1 constituent increased when using the spatially varying C_f map. The GEBCO_2014 bathymetry model gives lower $\overline{D}_{tg}$ than the SRTM15_PLUS model, however $\overline{D}_{tpx}$ are quite similar between the two bathymetric datasets. Note that $\overline{D}_{tpx}$ tends to give a smoother indicator of the change between model setups because it is integrated over the whole domain (where $25 < h < 500$ m). Furthermore, $\overline{D}_{tpx}$ is 2.9 cm or $\sim$30% smaller than $\overline{D}_{tg}$ for M_2. This could be because the shelf gauges tend to be in regions with large tidal ranges such as the northern regions of the Australian shelf and the Yellow Sea.

In comparison to other forward hydrodynamic models the performance is favorable. Stammer et al. (2014) reports that the global M_2 RMSE in shelf waters is 24-49 cm against tide gauges and 19-28 cm versus TPXO8. Comparatively, the M_2 RMSE is 13.1 cm against tide gauges and 10.1 cm versus TPXO8 for the *Comp + IT + SV* model setup. Although it should be kept in mind that the Stammer et al. (2014) errors are global and hence they cannot be treated as a direct comparison, according to the TPXO8 atlas the total energy density (TED, defined in §5.1) of the M_2 tidal wave is slightly higher in the IndWPac domain (820 Jm^{-2}) compared to the entire globe (695 Jm^{-2}). So while data-assimilation clearly provides greater accuracy on the continental shelf than forward hydrodynamic models can currently manage, computational grids that become fine enough to adequately support high-resolution bathymetric data nearshore and on the shelf (as in the IndWPac model) do appear to result in noticeably smaller errors than coarser forward hydrodynamic models.

4.5.3 Discrepancy at the Coast

The RMS discrepancies at the coastal tide gauges are only marginally larger than those on the shelf for the *Comp + IT + SV* model setup. However, the discrepancies increase significantly from the shelf to the coast when only the global bathymetry datasets are used, in particular GEBCO_2014. The nearshore bathymetry dataset plays a large role in reducing the discrepancy (30% reduction in total free surface $\overline{D}_{tg}$). The spatially varying C_f map has a smaller but noticeable global effect (9% reduction in total free surface $\overline{D}_{tg}$). Local effects of C_f are detailed in §5.4. At approximately 77% of the tide gauge locations the total free surface $\overline{D}_{tg}$ of the *Comp + IT + SV* model setup is less than 20 cm (Fig 7). This is the same as the target metric used for a high-resolution western North Atlantic model (much smaller in scale to IndWPac) where this was satisfied at 324 of 398 (81%) locations (Technology Riverside Inc. and AECOM, 2015).

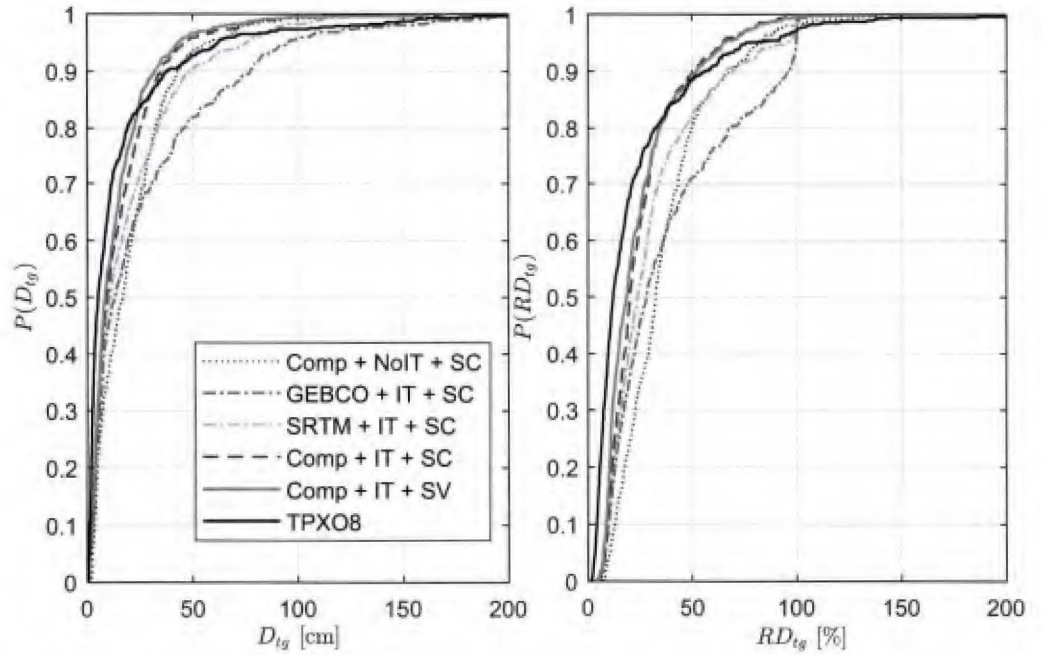

Figure 7: Cumulative distribution functions of the total free surface (up to all eight tidal constituents) RMS discrepancies D_{tg} (left), and relative RMS discrepancies RD_{tg} (right), versus coastal tide gauges for different IndWPac model setups (see explanation in footnotes of Table 4) and the TPXO8 atlas.

Even though the total free surface $\overline{D}_{tg}$ for the *Comp + IT + SV* model setup is 2.5 times that of the TPXO8 atlas on the shelf, $\overline{D}_{tg}$ is 2.6 cm (15%) smaller than the TPXO8 atlas for the *Comp + IT + SV* model setup at the coast. However, as illustrated by the cumulative distribution (cdf) curves (Fig 7), a higher percentage of locations will be within a given target discrepancy up to $\overline{D}_{tg}$ = 24 cm ($\overline{RD}_{tg}$ = 35%) for the TPXO8 model. On the other hand, the TPXO8 model cdf curves have long tails indicating a number of high-magnitude outliers, whereas this is not the case for the IndWPac model with the nearshore bathymetry included. A related trend is also evident: while $\overline{D}_{tg}$ for the *Comp + IT + SV* model setup model at the coast is only marginally increased from those on the shelf (and even decreased for K_1), $\overline{D}_{tg}$ for the TPXO8 atlas has increased almost two-fold for K_1 and five-fold for M_2. Furthermore, the standard deviations of $\overline{D}_{tg}$ for TPXO8 are much larger than $\overline{D}_{tg}$. In contrast, the standard deviations of $\overline{D}_{tg}$ for the IndWPac model setups using our comprehensive bathymetric data are similar in magnitude to $\overline{D}_{tg}$.

The total free surface $\overline{RD}_{tg}$ are slightly smaller for the TPXO8 atlas (23%) than the *Comp + IT + SV* model setup (24%). Furthermore, the IndWPac model cdf curves for RD_{tg} start off flat and begin from a higher minimum value than those of the TPXO8 atlas, whereas this is not the case for the D_{tg} curves. This could be explained by the difficulty in obtaining accurate relative discrepancies in regions of small tides especially those near amphidromes, e.g. in southern Australia RD_{tg} becomes large due to misplacement of the amphidrome off the southwest tip of Australia even though D_{tg} remain somewhat small (Fig 5). Free surface elevations associated with amphidromes that are situated offshore like this can be better placed through data-assimilation by e.g. TPXO8.

Overall, the large numbers and magnitudes of outliers and standard deviations of RMS discrepancies likely indicate that the TPXO8 atlas is unable to capture small-scale changes in amplitude

and/or phase that can occur in bays and harbors or in-behind small islands and peninsulas due to coarse resolution and bathymetry. But since TPXO8 cdf curves rise quickly initially, there is an indication that in coastal regions where the solution is not significantly different from that offshore (and where the gauges have been included in the assimilation process) TPXO8 is accurate. However, although TPXO8 use 1/30° resolution local insets to improve the coastal solutions, even finer computational grids on the coast that support high-resolution local bathymetry may be required to make further inroads into coastal performance elsewhere, particularly where nonlinearities play an important role (c.f. Lefevre, Provost, and Lyard, 2000; Lyard et al., 2006).

In contrast, the statistics indicate that the high-resolution computational grids and bathymetric data included in our model leads to the ability to better capture the faster changing characteristics of tides (particularly semi-diurnal ones) hence there are fewer large magnitude outliers and a smaller mean discrepancy compared with the TPXO8 atlas. However, at a high percentage of locations, TPXO8 gives smaller discrepancies because the IndWPac model suffers from a larger residual discrepancy coming from the offshore dynamics due to the absence of data-assimilation. If data-assimilation is not involved, then it would appear that significant improvements in offshore bathymetric data and internal tide dissipation dynamics need to occur to elevate the median performance at the coast in large-scale models. The following sections describe the sensitivities to these and other factors.

5 Sensitivities to Lateral Boundary Conditions, Bathymetry, and Dissipative Controls

5.1 Lateral Boundary Conditions

In this study it was found that the most dramatic effect on the solution occurred when modifying the position and/or lateral boundary condition type (Fig. 8). It turns out that the boundaries used in the final IndWPac model (which we call the 'two open boundaries domain' in this section) are fairly well placed. In the initial stages of the IndWPac model, the domain was set up so that the Western Pacific boundary was split into two separate boundaries where one of the boundaries was defined spanning from the Great Australian Bight down to Antarctica parallel with latitude (designated as the 'three open boundaries domain'). To evaluate the effect of the lateral boundary we quantify the total energy density, TED of the kth tidal wave:

$$TED^k = \frac{\rho_0 \iint \left(h|\boldsymbol{U}^k|^2 + g(A^k)^2 \right) \, dA}{2 \iint dA} \tag{15}$$

where ρ_0 is the reference density of sea water. A total of four simulations are conducted: the two open boundaries domain with and without an absorption-generation sponge layer, and the three open boundaries domain with and without a sponge layer. Note that none of these simulations use internal tide dissipation and a spatially constant $C_f = 2.5\times10^{-3}$ is employed.

5.1.1 Boundary Placement Effects without Sponge Layer

For simulations without the sponge layer, $TED^{\mathrm{M}_2} = 899$ Jm^{-2} for the two open boundaries domain and 3210 Jm^{-2} when using the three open boundaries domain, representing a 247% increase. For comparison, in the TPXO8 model $TED^{\mathrm{M}_2} = 820$ Jm^{-2} within the two open boundaries domain. The 79 Jm^{-2} excess in total energy density between the two open boundaries domain solution

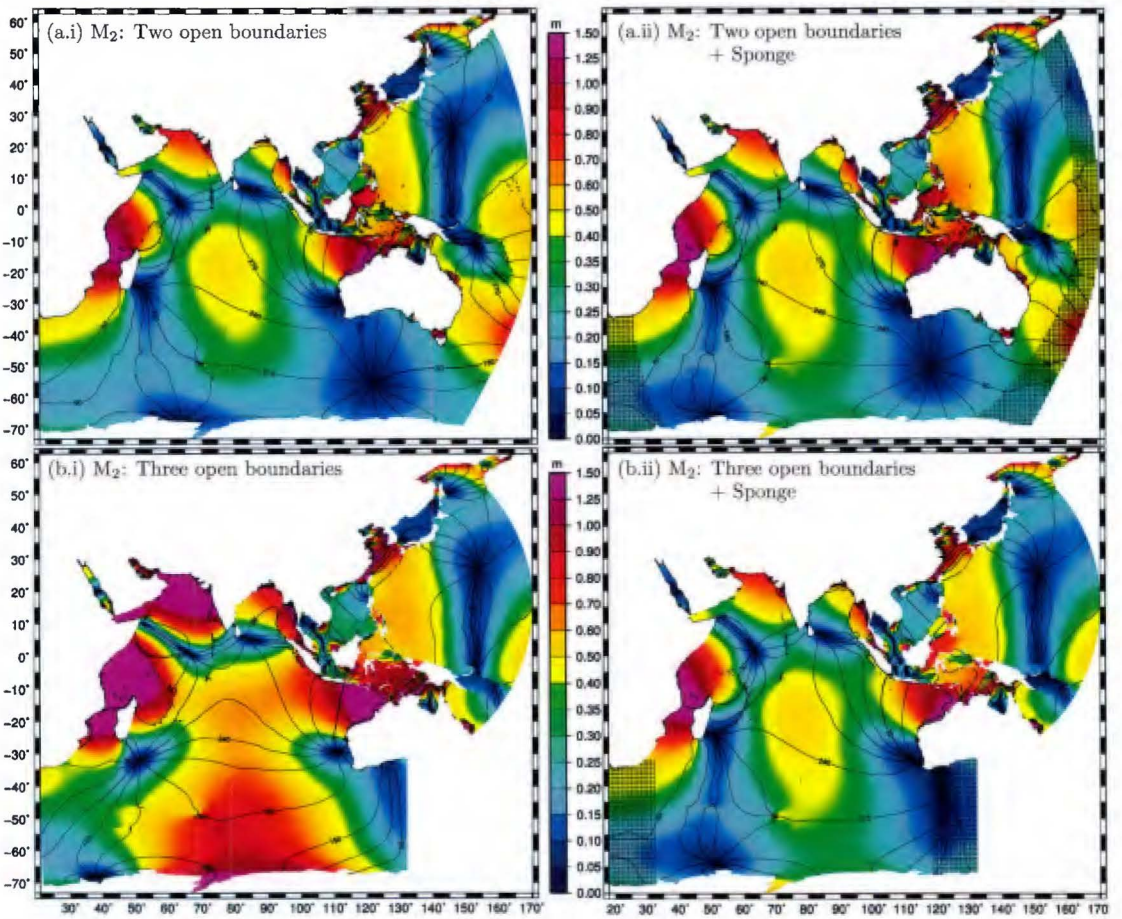

Figure 8: Responses of the M_2 tidal wave with no internal tide dissipation, and spatially constant C_f = 2.5×10^{-3}; (i) no absorption-generation sponge layer, (ii) with absorption-generation sponge layer ('+' hatched regions indicate sponge layer), (a) two open boundaries domain, (b) three open boundaries domain.

and TPXO8 can be explained, in part, by the absence of internal tide dissipation. The effect on the solution due to boundary placement was not nearly as prominent for the diurnal K_1 tidal wave. $TED^{K_1} = 288$ Jm^{-2} for the two open boundaries domain and 298 Jm^{-2} for the three open boundaries domain, representing a small 3.5% increase. Most other constituents also showed single digit percent increases except for the other two lunar semi-diurnal tides, K_2 and N_2. In particular, K_2 whose response is most similar looking to M_2, saw a 231% increase. N_2 was increased by 31.4%.

5.1.2 Effects of Sponge Layer

It was found that applying the absorption-generation sponge layer even for the three open boundaries domain can result in improved responses (Fig. 8 (b.ii)) reducing TED^{M_2} to 1040 Jm^{-2}. The sponge layer thus allows for significant leeway in boundary positioning but it does not necessarily entirely eliminate issues in the response. Note how in the two open boundaries domain the amphidrome in the Southern Ocean below Australia is located near where the third open boundary is. The sponge acts to push this amphidrome away from the boundary because the three open boundaries IndWPac model solution and the TPXO8 solution are incompatible here. This indicates reliance on internal dissipative mechanisms to ensure compatibility with each other.

5.1.3 Discussion

What to make of the dramatic results to the solution due to boundary placement and condition types? Firstly, even though there should not be an amphidrome right next to the boundary according to the TPXO8 solution (although the elevations are still fairly small), our model without adequate internal dissipative effects expects there to be one. Instabilities and problems may arise near amphidromes because a physically incorrect solution that satisfies the governing equations can be obtained. Mathematically, both boundary conditions and initial conditions are required to get the correct solution. Instead, the method commonly adopted (including this study) is to impose the elevation boundary conditions and ramp up the system from a completely zero state. We found from a simple test case that when internal dissipative effects are low, ramping generates spurious modes that persist for very long periods of time. Secondly, clearly the Indian Ocean and the Australian/Indonesian marginal seas appear very sensitive to fluctuations in fluxes on the boundary. As noted by Zahel and Müller (2005) in their study of free barotropic oscillations, the 11.65 hour resonant mode shows a very similar pattern to the lunar semi-diurnal tides in the Indian Ocean. Furthermore, the energy density of this mode is 2.2 times the global average in the Indian Ocean. Hence the resonant nature of the lunar semi-diurnal tides in this basin causes TED to increase wildly in response to the poor boundary conditions.

However, one of the main issues with using the absorption-generation sponge layer is the reliance on the reference solution. In particular, the fluxes obtained from TPXO8 are less likely to be as accurate or compatible with the IndWPac model as the TPXO8 elevations (because TPXO8 only assimilates elevations). We found an interesting case in our model where the solution near the southwest boundary degrades qualitatively versus the TPXO8 solution when implementing the sponge layer for the current two boundary domain (Fig. 8 (a.ii)). It is also shown in §5.3 that dissipation in the IndWPac model is slightly negative over a wide region of the Southern Ocean which could be due to the boundary conditions. Perhaps differences in fluxes are accentuated due to the skewness of the projection at high-latitudes. Additionally, in the Southern Ocean progressive waves are allowed to freely propagate around the globe suggesting that fluxes exiting the boundaries here would otherwise be allowed to enter the opposite boundary eventually leading to some equilibrium condition (that may be somewhat different than TPXO8) in a global model.

5.2 Bathymetry

Bathymetry is a boundary condition for oceanic models hence its importance to the solution is clear. Recent years have shown marked improvements in global bathymetric databases such as SRTM15_PLUS and GEBCO_2014. This section begins by outlining the effects of using one of these databases over the other, followed by effects between SRTM15_PLUS and our more comprehensive bathymetric data (Table 1). The section concludes with a discussion on the results and implications.

5.2.1 Comparisons between Global Bathymetric Databases

Current global bathymetric databases SRTM15_PLUS and GEBCO_2014 are good enough that they do allow us to obtain mean RMS discrepancies ~3 cm for the M_2 tidal wave in the deep ocean. Nevertheless, there is still a reasonable level of uncertainty between them (Fig 9). For example, on the abyssal hills the use of statistical roughness (Goff and Arbic, 2010) to calculate a new bathymetry set (Timko et al., 2017) has been undertaken to account for the effective coarseness of satellite altimetry derived bathymetry (note that the SRTM15_PLUS database used here is a combination with SRTM30_PLUS that contains the synthetic realization of the abyssal hill roughness but GEBCO_2014 is without it). To investigate the effects of the global bathymetric databases we compute one simulation using SRTM15_PLUS with abyssal hill roughness everywhere (*SRTM IT + SC*) and another using GEBCO_2014 everywhere (*GEBCO IT + SC*). RMS differences between the simulations for the M_2 tidal wave are plotted in Fig 9. Optimal internal tide dissipation factors (*IT*) and spatially constant $C_f = 2.5\times10^{-3}$ (*SC*) are employed for both.

Along the ocean ridges that include a synthetic realization of the abyssal hill roughness, the normalized bathymetric differences range between 5-25% except for the Southwest Indian Ocean Ridge where it can differ by more than 50% in spots. Despite this, M_2 RMS differences in deep water do not exceed 2 cm anywhere except east of Australia and New Guinea, i.e. the RMS differences between responses resulting from the two global bathymetric databases tend to be much less than RMS discrepancies between *Comp + IT + SV* model setup and TPXO8 (Fig 4 (c.i)). Note that although differences in the bathymetry should change the internal tide dissipation matrix, we used the same dissipation matrix as the *Comp + IT + SV* model setup for both simulations to help identify strictly *bathymetric* effects.

Major normalized bathymetric and RMS differences are unsurprisingly found in shallow waters such as the South China Sea, Bass Strait, Yellow Sea, Sea of Okhotsk, Ganges Delta, northern Andaman Sea, Persian Gulf, and the Gulfs of Khambhat and Kutch. The most astounding RMS differences are located on the northern Australian shelves, the Taiwan Strait and the Seto Inland Sea. In particular, the RMS differences in the Coral Sea and around Torres Strait are larger than the discrepancies between the *Comp + IT + SV* model setup and TPXO8. According to the sources of GEBCO_2014, the 2009 Australian Bathymetry and Topography Grid (Whiteway, 2009) is used around the Australian continent. Within this dataset, some of the nearshore bathymetry is made up of multibeam, Laser Airborne Depth Sounder, and nautical charts, with the rest based on 1 arc min and 2 arc min ETOPO satellite derived bathymetry. In comparison, SRTM15_PLUS is said to include 50 m multibeam datasets from 2012 as well as the Deepreef Explorer GBR dataset from 2010 (both newer than the 2009 Australian Bathymetry and Topography Grid).

5.2.2 Comparisons between SRTM15_PLUS and Local High-Resolution Bathymetry

Another issue with a global bathymetric dataset such as SRTM15_PLUS is that on the shelf and nearshore the resolution can be too coarse and it may contain holes in the bathymetry, thus it is not completely reliable for accurate regional simulations. This section outlines the differences

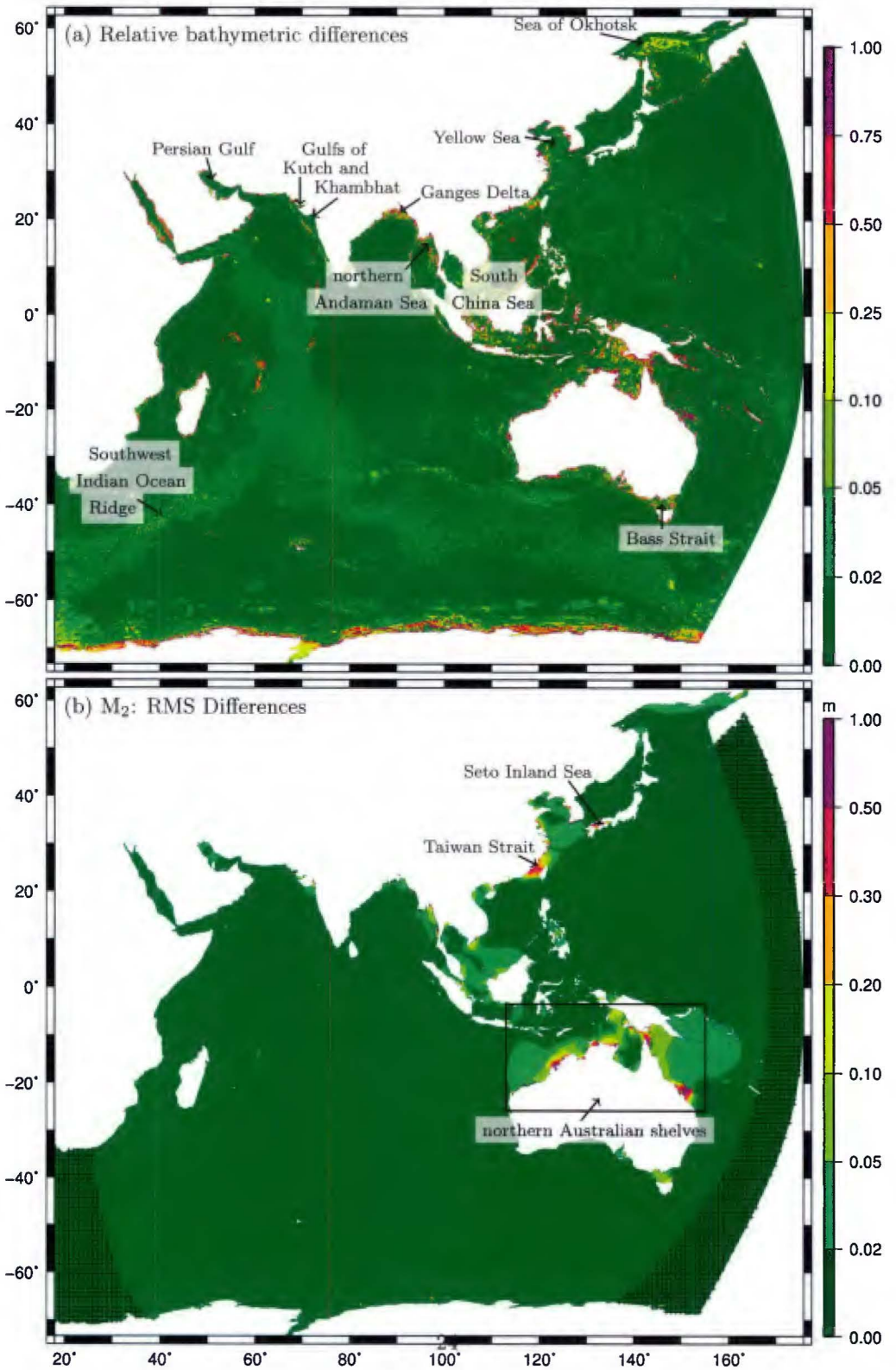

Figure 9: Differences between SRTM15_PLUS with abyssal hill roughness (Goff and Arbic, 2010) and GEBCO_2014 global bathymetric databases. (a) Normalized differences in the bathymetry, (b) M_2 RMS differences in the responses between the *GEBCO IT + SC*, and *SRTM IT + SC* model setups (see Table 4 for description of model setups).

between SRTM15_PLUS and our more comprehensive bathymetric data (Table 1) containing local high-resolution datasets. We focus on three regions: the East China Sea including the Yellow Sea and southern Japan; the South China Sea including the Philippines Seas and north Java Sea; and the Coral Sea including the Torres Strait (Fig 10).

All nearshore areas in the East China Sea show significant normalized bathymetric differences aside from Hong Kong which contains our smallest element sizes. Due to numerous spurious large depths in the SRTM15_PLUS dataset in this region we had to replace this area with the local high-resolution bathymetry in order to avoid instabilities due to violation of the CFL condition. This is not thought to have a large effect on the results of the comparisons between the bathymetric datasets and the conclusions that we draw from them. The simulations show large RMS differences of the M_2 tidal wave in the Taiwan Strait and Seto Inland Sea but interestingly they are not as large as those between GEBCO and SRTM15_PLUS, nor are differences in the Gulf of Tonkin as pronounced. It should be mentioned that we did notice reduced discrepancies at tide gauges in the Seto Inland Sea when using the high-resolution bathymetry. It is a complicated region with many small islands and channels and requires accurate connectivity of the energy fluxes to improve results. Most of the RMS differences in the Yellow Sea between SRTM15_PLUS and the local high-resolution bathymetry are larger than those between GEBCO and SRTM15_PLUS, in particular north of Shanghai and in the Incheon area. However, generally these differences are smaller than the discrepancies between TPXO8 and the *Comp + IT + SV* model setup.

Despite widespread normalized bathymetric differences in the Philippines and the region between the South China Sea and Java Sea, fairly small RMS differences in the M_2 tidal wave result aside from a few channels near Singapore, and in the gulfs near Batang Lupar and North Kalimantan, both on Borneo. This is perhaps partly because the M_2 amplitudes are relatively small in the region between the South China Sea and Java Sea. The larger K_1 (not shown) shows up to 10-30 cm RMS difference in the area south of Singapore but is not notable elsewhere. In the two gulfs on Borneo, which have fairly large M_2 tidal ranges (up to 1.7 m in the gulf near Batang Lupar), the differences result not only from local high-resolution bathymetric datasets but due to hand-edits vis-à-vis FUGAWI navigational charts. Areas like the gulf near Batang Lupar can be extremely sensitive to bathymetry particularly deep in the gulf where the v-shape concentrates the tidal energy. The effect of our hand-edits was to deepen the area near Batang Lupar allowing the tidal range to reach close to the measured one.

The final region is the Coral Sea which demonstrably shows large widespread normalized bathymetric differences. This is slightly perplexing as SRTM15_PLUS should include the Deepreef Explorer GBR dataset according to their references (`ftp://topex.ucsd.edu/pub/srtm15_plus/`). However, the SRTM15_PLUS version used in this study does not seem to have it incorporated. The bathymetry in the Torres Strait and Papua New Guinea region is also very different from SRTM15_PLUS, where we have actually used GEBCO_2014 in our more comprehensive bathymetric dataset. This is because GEBCO_2014 matches rather well with Deepreef Explorer GBR at the interface whereas SRTM15_PLUS does not. The resulting M_2 RMS differences shown here are certainly large and often well exceed those discrepancies between our model and TPXO8. In fact, in most of the Coral Sea the *Comp + IT + SV* model setup is performing rather well with respect to TPXO8 which could be largely attributed to the Deepreef Explorer GBR dataset. Fairly large discrepancies for our model against TPXO8 and tide gauges are still present near the Torres Strait where opposing M_2 energy fluxes meet over the strait (Fig 11, the definition of energy flux density, $\boldsymbol{P}$ is presented in §5.3). The residual discrepancy here is likely a combination of the remaining uncertainties in the GEBCO_2014 bathymetry (based on 2009 Australian Bathymetry and Topography Grid), and bottom friction dissipation.

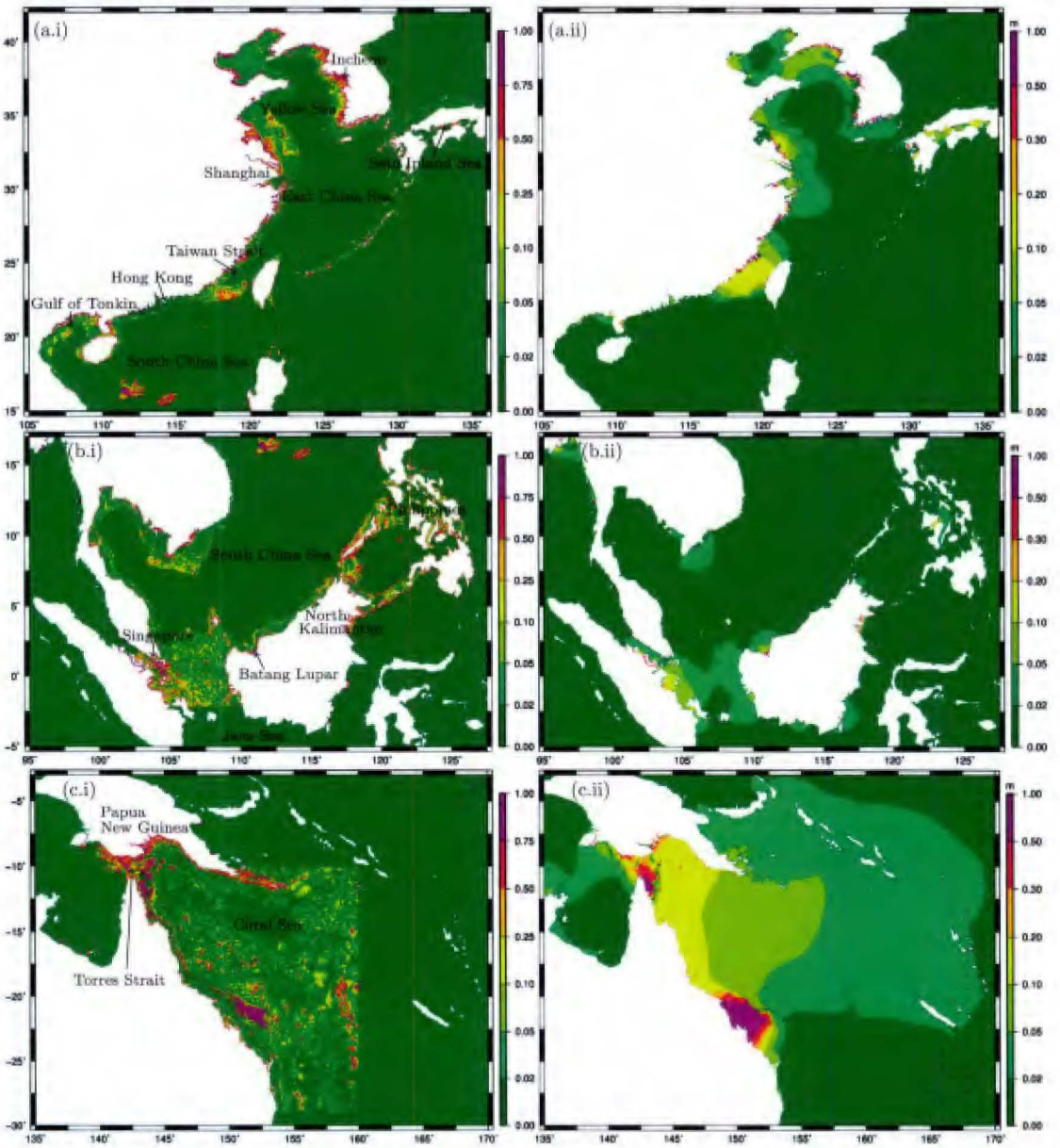

Figure 10: Differences between SRTM15_PLUS with abyssal hill roughness (Goff and Arbic, 2010) and our comprehensive bathymetric data (Table 1) containing local high-resolution datasets. (i) Normalized differences in the bathymetry, (ii) M_2 RMS differences in the responses between *SRTM + IT + SC* and *Comp + IT + SC* model setups (see Table 4 for description of model setups). (a) East China Sea, (b) South China Sea, (c) Coral Sea.

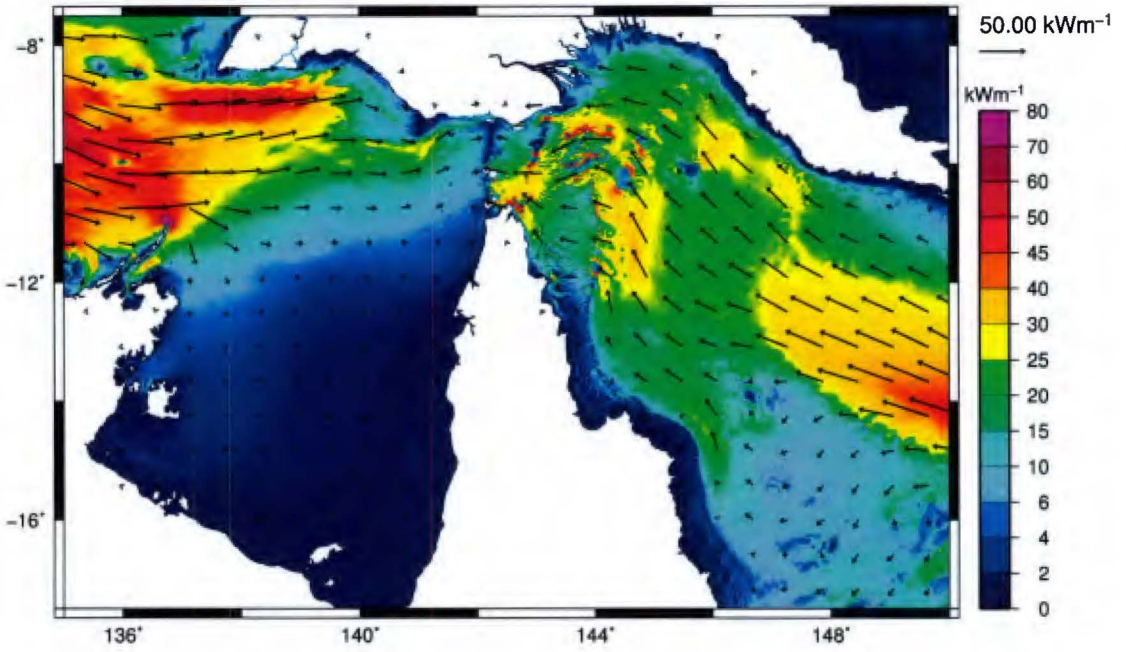

Figure 11: Energy flux density $\boldsymbol{P}$ of the M_2 tidal wave over the Torres Strait.

5.2.3 Discussion

The effect of different bathymetric datasets is not shown to be an important factor in the deep ocean, but on the shelf and nearshore there are certain regions where bathymetry plays a large role. This was also highlighted in terms of the global RMS discrepancies presented in §4.5 (summarized in Table 4). In some cases the RMS differences between simulations using different bathymetric datasets were greater than discrepancies between TPXO8 and the *Comp + IT + SV* model setup, particularly between the two global bathymetric datasets. Our more comprehensive bathymetric data and SRTM15_PLUS are mostly the same except nearshore in certain regions which was likely the reason for smaller RMS differences in general.

As discussed in Zaron (2017), bathymetry has the potential to control the tidal elevation particularly through resonant effects that are in general nonlocal. For example, the effect of the Deepreef Explorer GBR high-resolution bathymetry was to change the M_2 elevation over a large area beyond the Coral Sea out into the deep ocean. Conversely only small changes were noted throughout the region between the South China Sea and Java Sea. More locally, in a resonant basin such as the gulf near Batang Lupar, hand-edits of the bathymetry based on FUGAWI navigational charts allowed the tidal elevation to reach close to the measured M_2 amplitude. Clearly, greater availability and quality of nearshore and shelf bathymetry has the potential to greatly improve the modeling not only of tides but all shallow water flows.

With regards to the effect of the bathymetry in the deep ocean, it should be noted that bathymetry will affect internal tide dissipation as the dissipation matrix is based on topographic depths and slopes. So technically, the deep ocean may be more impacted than is shown here taking this aspect into account. Nevertheless, addition of the abyssal hill roughness, for example, has only marginally

increased the fidelity of ocean models (Buijsman et al., 2015; Timko et al., 2017). In 3D baroclinic models (Timko et al., 2017) this can be explained in part by limitations of resolution. On the other hand, 2D barotropic models such as IndWPac can achieve high-resolution over a wide-scale, but may be somewhat limited by the underlying assumptions of internal tide dissipation no matter the bathymetric data. Greater discussion on this aspect is presented in the next section.

5.3 Internal Tide Dissipation

In the two internal tide dissipation parameterizations (§3.3), it is necessary to calibrate a global amplification factor due to unknowns involved with the resolution of the bathymetric data and the way in which dissipation that is overestimated at supercritical slopes is handled, due to their linear assumptions. In addition to finding these amplification factors, this section discusses the differences between the two parameterization methods, introduces multiplier coefficients due to semi-diurnal resonance in the Luzon Strait, and concludes with some final remarks on reasons for differences between the methods and remaining issues for the parameterization of internal tide dissipation.

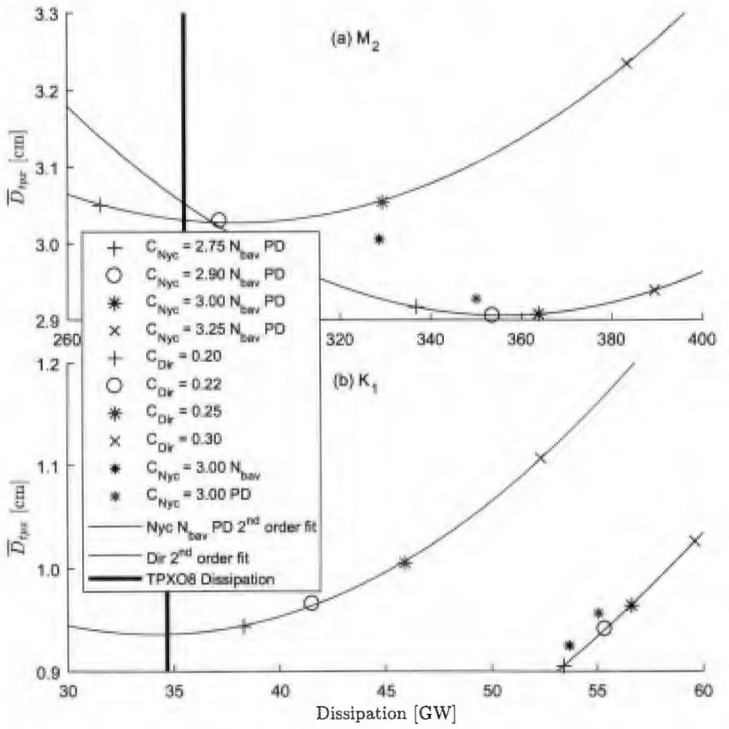

Figure 12: Total dissipation TD versus RMS discrepancy against TPXO8 $\overline{D}_{tpx}$ in deep water ($h > 500$ m) for different internal tide parameterization methods (*Nycander* and *Directional*) and amplification factors (C_{Nyc} and C_{Dir} respectively) with 2^{nd} order polynomial fits; (a) M_2 tidal wave, (b) K_1 tidal wave. *Nycander* method without positive definite (PD) or N_b spatial averaging (N_{bav}) modifications, and TPXO8 dissipation in deep water are shown for reference.

5.3.1 Calibrating Amplification Factors

We begin by trying to determine the optimal values of C_{Nyc} and C_{Dir} for the IndWPac model before comparing the performance of both parameterization methods. This is evaluated by looking at $\overline{D}_{tpx}$ for the M_2 and K_1 tidal waves in deep water ($h > 500$ m) with a spatially constant bottom friction, $C_f = 2.5\times10^{-3}$. To a lesser degree we are also interested in the total dissipation TD of individual tidal waves:

$$TD = \iint (W - \nabla \cdot \boldsymbol{P})\, dA \tag{16}$$

$$W = \frac{g\rho_0 h}{T} \int_0^T \boldsymbol{u} \cdot \nabla(\eta_{EQ} + \eta_{SAL})\, dt \tag{17}$$

$$\boldsymbol{P} = \frac{g\rho_0 h}{T} \int_0^T \boldsymbol{u}\eta\, dt \tag{18}$$

where, W is the work rate, and $\boldsymbol{P}$ is the energy flux. Since the numerical calculation of $\nabla \cdot \boldsymbol{P}$ with finite precision is very noisy, in this work the area-integral is computed using the divergence theorem. Comparisons of $\overline{D}_{tpx}$ versus TD in deep water for the individual tidal waves are shown in Fig. 12 using four different values of amplification factors for each method.

Regarding the K_1 tidal wave, amplification factors slightly smaller than the values tested appear optimal in both parameterization methods. However, we focused on the results of the M_2 tidal wave to determine the optimal amplification factors. This led to $C_{Nyc} \approx 2.9$ and $C_{Dir} \approx 0.22$ based on a second-order polynomial best fit. For comparison, Buijsman et al. (2015) determined $C_{Nyc} \approx 2.75$, which is in fairly close agreement. Furthermore, two modifications were applied to the *Nycander* method. The first modification simply ensured that the dissipation matrix was positive definite (PD). A second modification involved applying Gaussian smoothing of N_b (to obtain a variable denoted as N_{bav}) using the same radius and scaling as the convolution integral for J, the argument being that nonlocal effects of buoyancy may be just as important as nonlocal effects of topography. Both modifications create more dissipation and makes $\overline{D}_{tpx}$ for M_2 smaller for the same value of C_{Nyc} (Fig. 12), with the PD modification having the largest effect.

5.3.2 Differences between Parameterization Methods

Two opposing outcomes result from the comparison between the *Nycander* and *Directional* methods. For both constituents the *Nycander* method leads to slightly smaller values of $\overline{D}_{tpx}$, while TD at the optimal amplification factor matches TPXO8 in deep water more closely for the *Directional* method. For the reason that TPXO8 can be reliably validated for elevations but not for dissipation we are inclined to the prefer the *Nycander* method, thus it is incorporated into our best model results presented in §4. It is however worth pointing out that the difference between the methods is no more that 15 mm in $\overline{D}_{tpx}$ for M_2, thus the *Directional* method can be considered a very useful parameterization in its own right - not least because it can be quickly calculated and introduced to a numerical model.

With regards to total dissipation, the optimal *Nycander* method results in 24% greater M_2 TD compared with TPXO8, which is in very close agreement to the HYCOM global model (23% larger than TPXO8) (Buijsman et al., 2015). Buijsman et al. (2015) notes that the TPXO8 dissipation rates are diffused over large areas in comparison to the parameterized internal tide dissipation in their model. In that sense it is somewhat unclear how reliable TPXO8 dissipation in deep water may be. Issues with tidal dissipation in global data-assimilated models have been previously highlighted

(Lyard et al., 2006; Le Provost and Lyard, 1997), and there are large regions of negative dissipation rates when computing this with the TPXO8 solutions.

To get a sense of the global differences in the way the two methods dissipate energy and affect the response, plots of the dissipation density ($W - \nabla \cdot \boldsymbol{P}$) for M_2 between the optimal *Nycander* and *Directional* methods are shown in Fig. 13. The spatial distribution is similar to previous studies (e.g Green and Nycander, 2013; Buijsman et al., 2015). In the deeper regions such as the abyssal hills (namely the West Indian Ocean Ridge and Western Pacific Trench), the general observation is that the *Nycander* method focuses dissipation towards the center peaks of the ridges whilst the *Directional* method tends to spread dissipation over the width of the ridge. This makes sense because the *Directional* method is a function of the square of the local topographic gradient meaning that dissipation may be triggered locally more easily than the *Nycander* method which requires both a

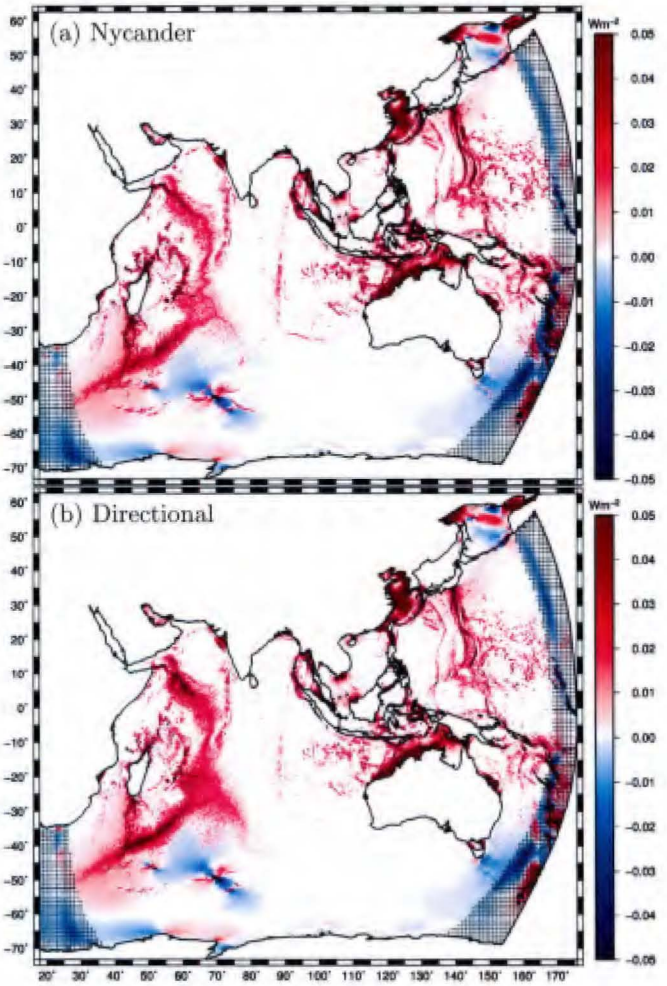

Figure 13: Dissipation density of the M_2 tidal wave comparing internal tide dissipation methods; (a) *Nycander* method (PD and N_{bavg} corrections) with $C_{Nyc} = 2.90$, (b) *Directional* method with $C_{Dir} = 0.22$. '+' hatched regions indicate sponge layer.

large local topographic gradient and a large gradient of J (which will be largest in the center or ridges as it is a measure of the overall topographical change in the vicinity). This is true too for island chains where the *Nycander* method tends to give greater dissipation here because even if the local topographic gradients are not large, the topographical change in the general vicinity of the islands might be.

Depth-wise the characteristics of local and large-scale topographic gradients tend to translate into the *Nycander* method creating more dissipation in shallower depths (Fig. 14). Both methods give large amounts of dissipation in the 3000 - 4000 m range corresponding to abyssal hills, but the *Directional* method dissipation drops off more rapidly with decreasing depth to match TPXO8 surprisingly well in shallow depths < 500 m. As mentioned above, it remains unclear whether the overestimate in dissipation from both schemes in the 500 - 4000 m depth range (and underestimate in the 4500 - 6000 m range) is a major cause of concern or that it simply reflects the coarseness of the data-assimilated model. Buijsman et al. (2015) found similar trends (to this study) for their global model.

The differences in amplitudes of the M_2 tidal wave between the *Nycander* and *Directional* methods are illustrated in Fig. 15. There is a clear divide between amplitudes in the Indian Ocean and those in the Western Pacific Ocean. This indicates disparity in the way the M_2 tides are balanced between basins depending on the method. The *Nycander* method dissipates more in shallower depths

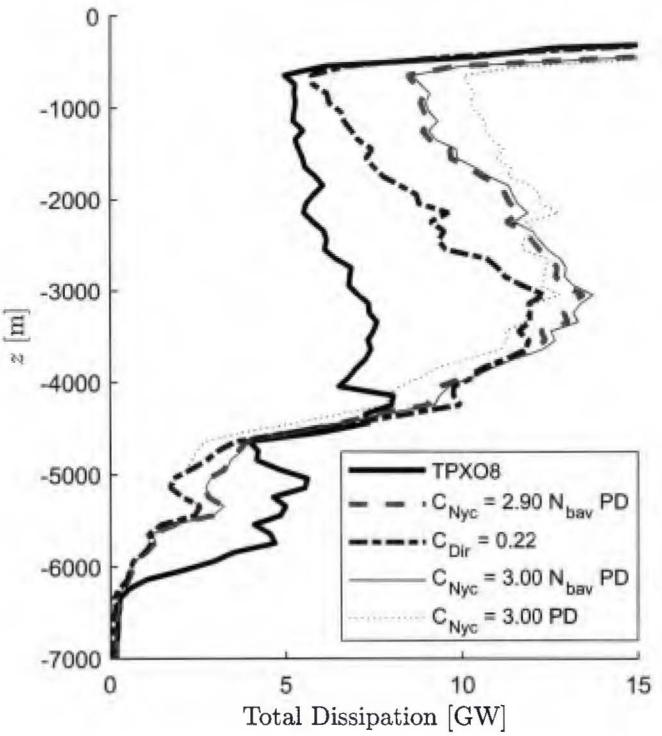

Figure 14: Bathymetric depth versus total dissipation TD (summed in 100 m depth bins) for the M_2 tidal wave comparing TPXO8 and the internal tide dissipation parameterization methods (modified *Nycander* and *Directional*) with their optimal amplification factors. *Nycander* method without the N_b spatial averaging modification (N_{bav}) is shown for reference.

(Fig. 14), so it is perhaps unsurprising that the amplitudes will be smaller in the Western Pacific basin which contains many shallow shelves and island chains. Moreover, the energy flux density $\boldsymbol{P}$ of the M_2 tidal wave predominantly flows from the Indian Ocean into the Western Pacific basin through the Indonesian Seas, and to a lesser extent through the Malacca Strait (Fig. 16). Due to the greater dissipation in shallow depths as it passes through the island chains and shallow seas, more energy remains on the Indian Ocean side instead of flowing into the Western Pacific basin compared with the *Directional* method.

5.3.3 Multiplier due to Semi-diurnal Resonance over the Luzon Strait

A local improvement to internal tide dissipation was applied over the Luzon Strait. The Luzon Strait controls the amount of energy into the South China Sea for both the M_2 and K_1 tidal waves (Fig. 16). Here, the amplitude of K_1 is mostly larger than M_2 (Fig 4). Because the separation of the double-ridge topography in the strait is similar to the semi-diurnal internal tide wavelength, it has been shown that resonance dramatically increases the barotropic to baroclinic energy conversion (Buijsman et al., 2014). In comparison to the sum of the two ridges considered separately, the

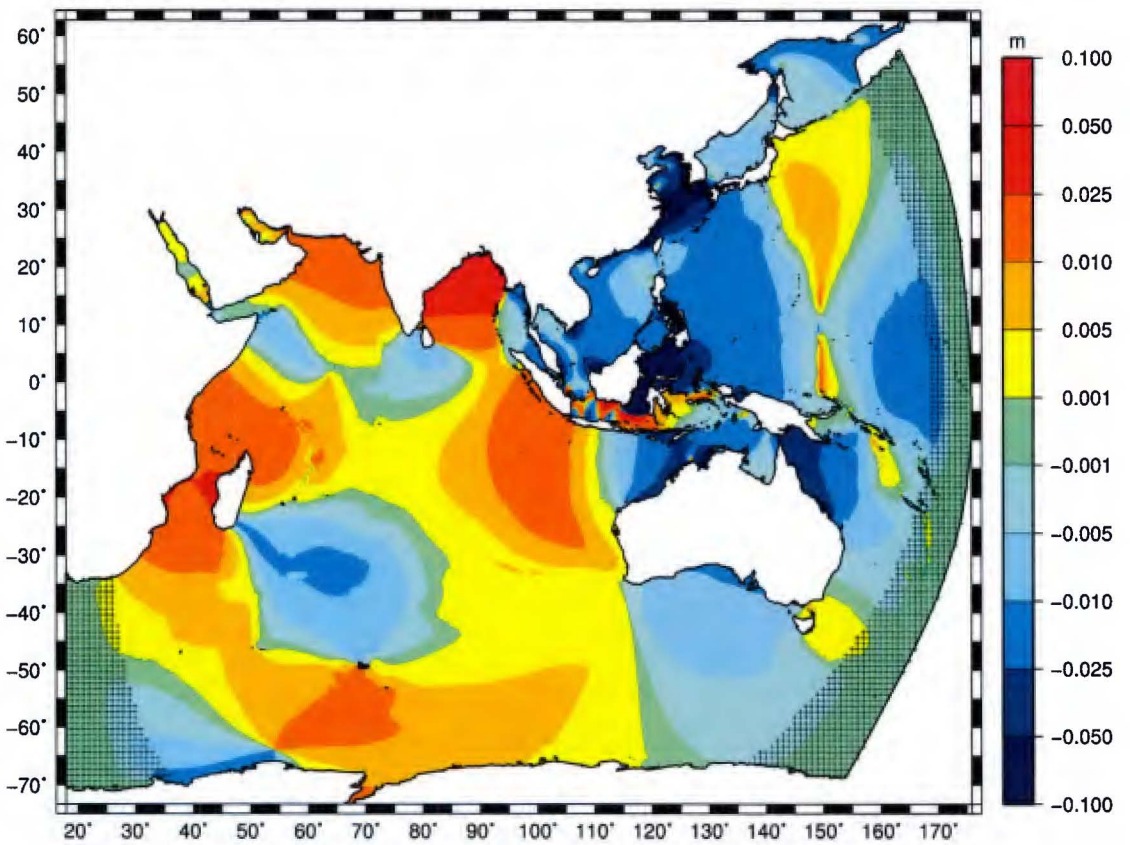

Figure 15: M_2 tidal wave amplitude differences between the two internal tide dissipation methods (modified *Nycander* method with $C_{Nyc} = 2.9$ minus the *Directional* method with $C_{Dir} = 0.22$).

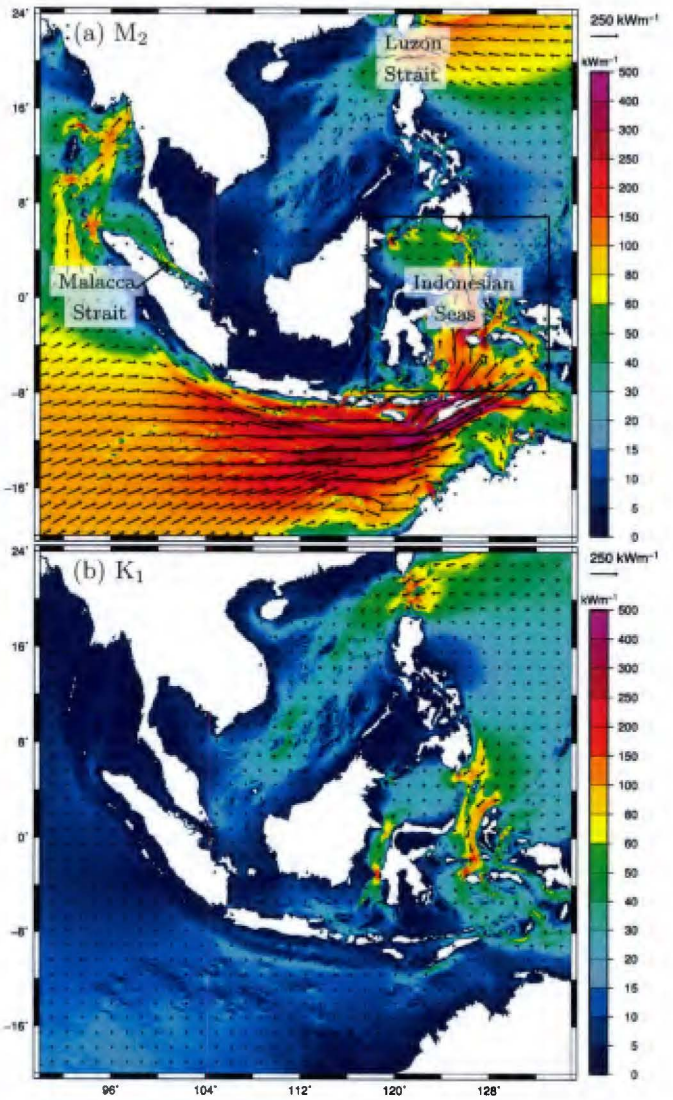

Figure 16: Energy flux density $\boldsymbol{P}$ of the (a) M_2 and (b) K_1 tidal waves in the marginal seas separating the Indian Ocean from the Western Pacific Ocean.

double-ridge produced up to as much as four times the energy conversion for the first-internal mode (Buijsman et al., 2014). Since our internal tide dissipation parameterizations do not include such resonance behavior we deemed it appropriate to apply a multiplier to the amplification coefficients in the region 19.5°-21.5°N and 120°-122.5°E. The multiplier coefficients C_{Luzon} were defined using a skewed Gaussian curve as a function of latitude ϕ to approximate the data-points presented in Buijsman et al. (2014):

$$C_{Luzon} = 1 + \frac{a_L}{2\sigma_L \pi} \exp\left(\frac{-\xi_L^2}{2\sigma_L^2}\right)\left[1 + \mathrm{erf}\left(\frac{\alpha_L \xi_L}{\sqrt{2}\sigma_L}\right)\right] \tag{19}$$

with a_L = 5.0, σ_L = 0.3, α_L = -1.0, and $\xi_L = \phi - 20.9°$N. C_{Luzon} reaches a maximum of 4.24 at 20.75°N.

Fig. 17 shows the amplitude differences for the M_2 and K_1 tidal waves in the South China Sea and surrounds between the optimal *Nycander* method with and without the multiplier coefficients C_{Luzon}. As expected, the increase to the internal tide coefficients reduces the amplitudes inside most of the South China Sea for both constituents. The decrease is on the order of 0.5-1 cm for M_2 in most areas with a few pockets of 2.5-5 cm reductions. Additionally, the blockage increases amplitudes slightly to the east of the strait and in the Sulu Sea. The K_1 amplitude is decreased in the South China Sea by 1-2.5 cm almost uniformly. Furthermore, due to the blockage at the Luzon Strait more of energy flux is now diverted down into the Indonesian seas (Fig. 16) increasing amplitudes uniformly by 0.5-1 cm.

M_2 RMS discrepancies at coastal tide gauges are generally decreased on the order of 1 cm within the South China Sea due to the C_{Luzon} multiplier coefficients. The discrepancy is increased slightly in the Sulu Sea and near the Taiwan Strait. The changes in K_1 discrepancies do not follow a clear pattern aside from in the Gulf of Thailand and Celebes Sea regions (decrease and increase respectively). The RMS discrepancies against tide gauges and TPXO8 in the plotted region (Fig. 17) are summarized in Table 5. Overall only small decreases in discrepancies are found when using the C_{Luzon} multiplier coefficients. However, the discrepancies compare rather favorably to a local hydrodynamic model for just the South China Sea region (Green and David, 2013) (we get 8.5 cm and 5.0 cm RMSE for M_2 and K_1 versus TPXO8 respectively, Green and David (2013) quotes 9 cm and 10 cm). In that study C_f had to be raised to an unphysical value of 0.01 to achieve

Table 5: The mean RMS discrepancies (units: cm) versus coastal tide gauges $\overline{D}_{tg}$ and TPXO8 $\overline{D}_{tpx}$ (in all depths) of the M_2, K_1, and the total free surface (up to all eight major constituents) within each of the regions plotted in Figs. 17 and 19. Standard deviations in parentheses. See Table 4 for model setup descriptions.

Region	Model	$\overline{D}_{tg}^{M_2}$	$\overline{D}_{tg}^{K_1}$	$\overline{D}_{tg}^{all}$	$\overline{D}_{tpx}^{M_2}$	$\overline{D}_{tpx}^{K_1}$	$\overline{D}_{tpx}^{all}$
SCS	*Comp + IT(LZ) + SV*	7.35 (6.75)	6.92 (5.88)	14.3 (10.2)	3.76 (7.56)	3.63 (3.37)	6.70 (10.4)
	Comp + IT(NoLZ) + SV	7.55 (6.63)	6.96 (5.73)	14.2 (10.0)	4.07 (7.53)	3.74 (3.56)	6.90 (10.4)
YS	*Comp + IT + SC*	17.2 (17.7)	3.74 (3.74)	20.8 (20.3)	8.58 (16.9)	1.70 (9.53)	10.3 (18.4)
	Comp + IT + SV	12.3 (15.6)	3.04 (3.31)	16.1 (17.7)	6.51 (17.1)	1.41 (9.81)	8.43 (18.2)
JS	*Comp + IT + SC*	10.5 (9.50)	5.98 (5.41)	16.5 (11.6)	6.02 (7.11)	5.47 (7.08)	10.6 (7.39)
	Comp + IT + SV	11.5 (10.8)	6.54 (5.39)	17.9 (12.6)	5.97 (7.05)	6.60 (6.66)	11.5 (7.58)
TAS	*Comp + IT + SC*	18.8 (24.6)	9.49 (8.16)	25.9 (28.2)	6.46 (9.68)	4.03 (8.50)	9.71 (11.1)
	Comp + IT + SV	19.9 (24.8)	10.2 (8.63)	27.6 (28.6)	6.81 (9.86)	4.28 (8.62)	10.3 (11.7)

*SCS: South China Sea region plotted in Fig. 17. LZ refers to the use of multiplier coefficients, C_{Luzon} from (19), over the Luzon Strait. NoLZ is without applying C_{Luzon}

*YS: Yellow Sea and southern Japan region plotted in Fig. 19 (i)

*JS: Area between the Java Sea and South China Sea plotted in Fig. 19 (ii)

*TAS: Timor and Arafura Seas region plotted in Fig. 19 (iii)

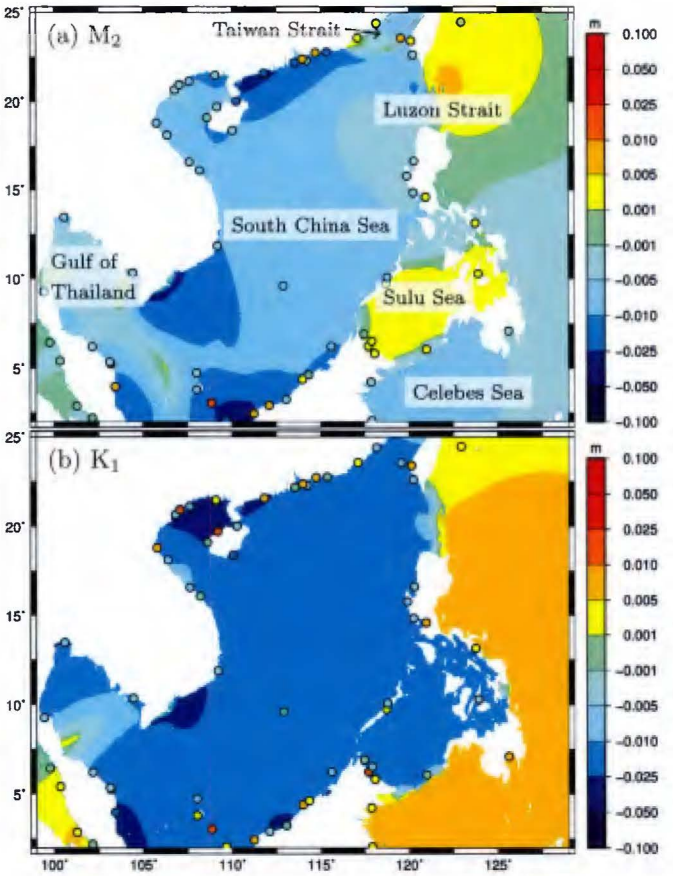

Figure 17: (a) M_2 and (b) K_1 amplitude differences in the South China Sea and surrounds when using the multiplier coefficients C_{Luzon} over the Luzon Strait (case with C_{Luzon} from (19) minus case without C_{Luzon} applied). Circles indicate the change in RMS discrepancies at coastal tide gauges (negative indicates reduction in discrepancy when using C_{Luzon}).

optimal results for M_2. It was speculated that this is because the internal tide dissipation rates in, e.g. the Luzon Strait, are underestimated for M_2. This may have been the case in Green and David (2013), but the results shown here indicate that using C_{Luzon} multiplier coefficients due to semi-diurnal resonance from the double-ridge only provides a marginal positive effect. One reason for the disparity between the two models could be that fluxes to the east of the Luzon Strait may be quite different since the Green and David (2013) model is driven by the TPXO8 solution at lateral boundaries close to the strait whereas our boundaries are much further away. Differences in bathymetry (SRTM15_PLUS and the inclusion of local high-resolution bathymetry in IndWPac, versus GEBCO_2014 in Green and David (2013)) also likely play a role in improved responses for the IndWPac model.

5.3.4 Discussion

As a result of the dissipation dynamics we found that the *Directional* method gave better results in the Western Indian Ocean, but elsewhere the *Nycander* method was generally preferable. It is worth noting that the M_2 amplitude differences (Fig 15) in the Indian Ocean between the two methods ranges between 0.5-2.5 cm, and more in the Bay of Bengal. This is a rather large amplitude difference in the deep ocean since $\overline{D}_{tpx} = 2.9$ cm, indicating that there is some scope to improve deep water solutions further through better parameterization of internal tide dissipation. Perhaps some of the remaining issues for the *Nycander* method can be explained by the fact that bathymetry is still rather uncertain and coarse in much of the deep ocean (most of the Indian Ocean is deep with very narrow shelves, and internal tide generation is an important dissipation mechanism). Furthermore, internal tide dissipation in shallow regions is less reliable because of larger tidal velocities and uncertainties, and there is a greater chance of the flow being supercritical (Melet et al., 2013). In fact, one of the main effects of the N_{bav} modification to the *Nycander* method was to move some dissipation away from shallow regions into deeper regions (Fig. 14). More investigation into the parameterization of internal tide generation in shallow regions is warranted especially because the shallow areas of the Indonesian seas provide a critical connection between the basins, a region that has created issues previously (Melet et al., 2013).

Finally, it is worth highlighting that the internal tide dissipation matrices used here have been derived based on the M_2 tidal wave. That is, $\omega = 2\pi/12.42$ rad/hr is used in (4) and (5), and the optimal amplification factors were determined from results for M_2. However, theoretically diurnal internal tides become trapped in latitudes higher than $\sim 30°$ and no barotropic to baroclinic energy conversion due to freely propagating internal waves would result. Because we apply the dissipation matrix for M_2, some dissipation of diurnal tides does occur at these higher latitudes in our model. However, without separating the modes and taking into account the influences from the other constituents similar to methods for bottom friction (e.g Le Provost and Lyard, 1997), it is unclear how selective dissipation for each mode is possible using this type of parameterization in a forward model. Our assumption for internal tide dissipation is that the M_2 tidal wave dominates the signal. Nevertheless, as shown in Fig. 12, smaller amplification factors are optimal for the K_1 tidal wave than those for M_2. Furthermore, in the Luzon Strait only resonance of the semi-diurnal internal tides occur so theoretically the multiplier coefficients C_{Luzon} should not be applied to the diurnal tides. Perhaps, including information from measurements and operational baroclinic 3D models, e.g. HYCOM (Chassignet et al., 2007), may provide us with an opportunity to locally improve dissipation matrices for depth-integrated barotropic models, although we are still somewhat limited by the assumptions of the underlying parameterization.

5.4 Bottom Friction Dissipation

This section summarizes the effect of implementing the spatially varying C_f map (Fig 3) based on sediment types and tidal current speeds into the IndWPac model. Firstly, it is useful to highlight regions where we expect bottom friction to have a large effect. Zaron (2017) recently introduced a bottom friction number, R_f for the k^{th} constituent to quantitatively illustrate this:

$$\left(R_f^k\right)^2 = \frac{\left(C_f u_f |\boldsymbol{u}^k|/h\right)^2}{\left(\omega^k |\boldsymbol{u}^k|\right)^2 + \left(C_f u_f |\boldsymbol{u}^k|/h\right)^2} \tag{20}$$

where ω^k is the tidal frequency of k^{th} constituent. The term ω^k corresponds to local acceleration. Since depth and velocities are highly correlated (velocity and C_f are to some extent also correlated but much less so) it is clear from (20) that the effect of C_f is in fact secondary to the effects of h.

Thus, a global map of R_f based on the spatially constant $C_f = 2.5\times10^{-3}$ simulation ought to suffice for visualization purposes (Fig 18).

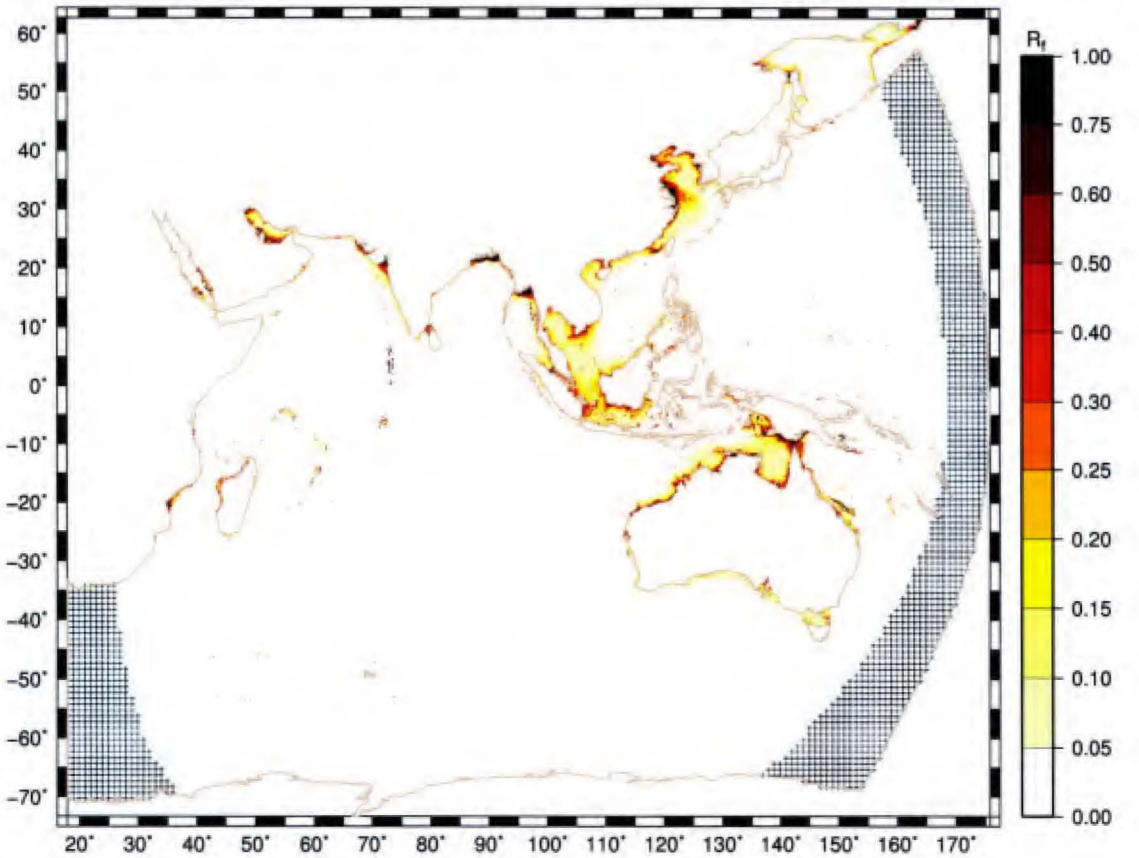

Figure 18: M_2 bottom friction number R_f based on the *Comp + IT + SC* model setup.

R_f shows a similar pattern for the K_1 tidal wave (not shown) as the plotted M_2 tidal wave. On the continental shelves at depths ~100 m, R_f is generally in the 0.1-0.5 range, and only becomes larger than 0.5 close to the coast in depths much less than 50 m (see also Zaron, 2017). Regions where R_f is large correlate to areas where the tidal solutions will be most impacted by any variability in C_f. When implementing the spatially varying C_f map (Fig 3), specific areas with relatively large R_f that are noticeably different to $C_f = 2.5\times10^{-3}$ include: the Yellow Sea and southern Japan (small C_f in Yellow Sea, large C_f just south of Yellow Sea and in the Seto Inland Sea); the area between the Java Sea and South China Sea near Singapore (mostly large C_f with pockets of small C_f); and Timor and Arafura Seas (both large and small C_f). The change in amplitudes for the M_2 and K_1 tidal waves in these three regions when using the spatially varying C_f map over the spatially constant $C_f = 2.5\times10^{-3}$ are illustrated in Fig 19. Changes in the RMS discrepancy at the coastal tide gauges are also plotted. The mean discrepancies at the coastal tide gauges within the boxed regions are summarized in Table 5. The following sections detail the findings at each region individually, followed by a discussion of the results.

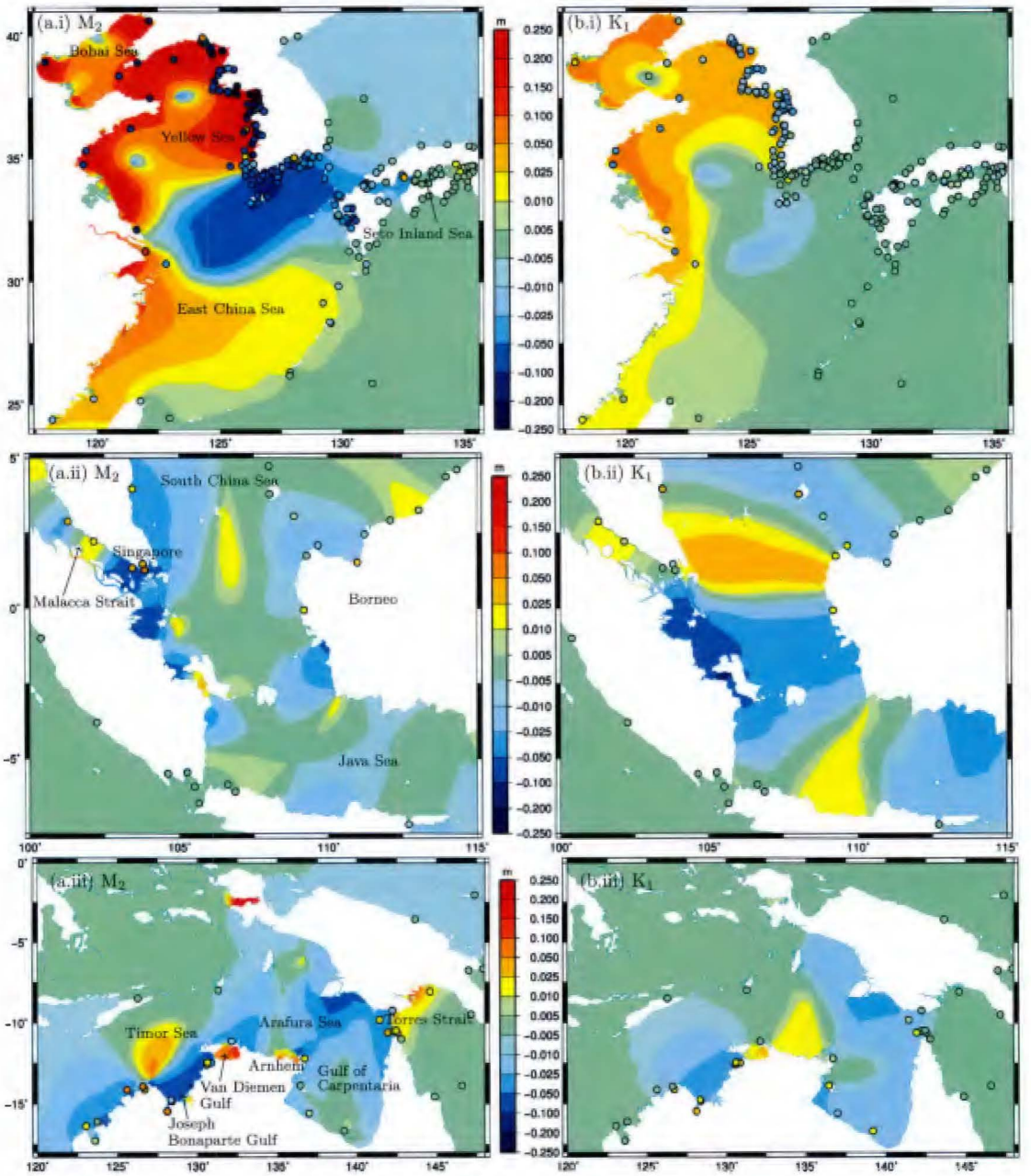

Figure 19: (a) M_2 and (b) K_1 amplitude differences due to changes in bottom friction coefficients C_f (case with spatially varying C_f map minus case with spatially constant $C_f = 2.5{\times}10^{-3}$). Circles indicate the change in RMS discrepancies at coastal tide gauges (negative indicates reduction in discrepancy for spatially varying C_f model setup); (i) Yellow Sea and southern Japan, (ii) area between the Java Sea and South China Sea, (iii) Timor and Arafura Seas.

5.4.1 Yellow Sea and southern Japan

In the census sediment database, the Yellow Sea (including Bohai Sea) is designated as a mud sediment type and the tidal currents are very large over the shallow basin. This leads to small values of C_f between 1.0×10^{-3} and 2.0×10^{-3}, except close to the coastline where C_f becomes large due to small depths in (6). A patch of sand just south of the Yellow Sea causes C_f to exceed 4.0×10^{-3} here. Additionally, a sand zone throughout most of the Seto Inland Sea induces a large C_f ($> 4.0\times10^{-3}$).

The tidal amplitudes increase due to the spatially varying C_f in most of the Yellow Sea, and decrease just south of the Yellow Sea due to the mud and sand zones respectively for both constituents. The M_2 amplitude is also decreased in the western Seto Inland Sea but there is no noticeable change for K_1. Impressively, the RMS discrepancy is decreased almost everywhere for both constituents aside from a couple of outliers in the Yellow Sea and for a group of stations in the eastern Seto Inland Sea for M_2. For example, the discrepancy is decreased by up to 25 cm and 5 cm for M_2 and K_1 respectively at many Yellow Sea locations. It appears the the combination of the small friction in the Yellow and Bohai Seas and the large friction just south of the Yellow Sea and in the Korea-Japan strait result in systematic positive changes to the solution. Overall, the mean RMS discrepancies versus coastal tide gauges decrease by 4.9 cm (28%) for M_2 and 0.71 cm (19%) for K_1 due to the spatially varying C_f here.

5.4.2 Area between the Java Sea and South China Sea

The region in between the Java Sea and South China Sea is predominantly designated as a sand zone ($C_f > 4.0\times10^{-3}$) with pockets of fine-grain calcareous sediment ($C_f \approx 2.0\times10^{-3}$) and volcanic ash ($C_f \approx 3.0\times10^{-3}$) in the census sediment database. There are only a small number of data-points in the census to back up these sediment types.

The M_2 amplitudes decrease most significantly in the region close to Singapore due to the higher values of C_f and R_f here. In response to this decrease in amplitude, the M_2 RMS discrepancies increase by approximately 5 cm here. A large scale decrease in K_1 amplitudes occur southeast of Singapore but there are no coastal tide gauges here to measure the effect on the discrepancy. A band of increased K_1 amplitude in between Singapore and Borneo which increases the RMS discrepancies at the tide gauges is also present. The mean total free surface RMS discrepancies are increased versus tide gauges by 1.4 cm (8.5%) overall (Table 5). Thus, increasing C_f from the base value of 0.025 to the sediment/current informed estimate clearly degraded the accuracy in both the semi-diurnal and diurnal constituents suggesting that either the census sediment database is not correct or that the high current speeds in the Malacca Strait artificially increase the friction coefficient for the sand sediment type. We believe that the comprehensive bathymetry in this heavily trafficked region is reliable in that it matches navigation charts well.

5.4.3 Timor and Arafura Seas

The Timor Sea is designated as a sand sediment type in the census sediment database while the Arafura Sea is designated as mainly fine-grained calcareous sediment with a couple of pockets of sand types. As a result, in most of the Timor Sea $C_f > 4.0\times10^{-3}$ except for nearshore in the Joseph Bonaparte Gulf where the tidal velocities are very large causing C_f to decrease here as the fine-grained sediment bedforms are washed out. The tidal velocities are fairly small in the Gulf of Carpentaria so even though some of sediment is fine-grained, C_f is similar to the standard value (2.5×10^{-3}). North of Arnhem the sediment is fine-grained and the tidal currents are fairly large hence C_f becomes smaller than the standard value.

Because most of the region has larger values of C_f than the standard value, tidal amplitudes tend to decrease for both constituents on the whole (Fig 19 (iii)). Exceptions are the Van Diemen Gulf (small C_f), north of Arnhem (small C_f nearshore with high C_f just offshore), and east of the Torres Strait, but only for M_2. The mechanism for the latter is mainly through dampening of the energy fluxes traveling east towards the Torres Strait as they encounter the sand zones in the Timor and Arafura Seas. This results in less resistance to the westward directed energy fluxes into the Torres Strait increasing amplitudes to the east of the strait (see Fig 11). In general, using the spatially varying C_f led to poorer results for both constituents. Only deep in the Joseph Bonaparte Gulf and at a couple of stations near the Van Diemen Gulf with smaller C_f values did the M_2 RMS discrepancy decrease. Mean total free surface RMS discrepancies at tide gauges increased by 1.7 cm (6.6%) due to the spatially varying C_f. Again, this could be related to the sediment information derived from the census sediment data or from the friction coefficient estimation. In addition, the degree of uncertainty of the bathymetry is high as explored in §5.2, which will substantially influence the dissipation and the energy fluxes.

5.4.4 Discussion

Results summarized in the above sections highlight one region (the Yellow Sea and southern Japan) that experienced wholesale decreases to the discrepancies at tidal stations by significant magnitudes, and two regions with small increases in discrepancies, when using the spatially varying C_f map over the standard $C_f = 2.5\times10^{-3}$. The Yellow Sea region represents a flagship result of the possibilities of using a data-informed approach to estimating bottom friction coefficients over using a standard value. Furthermore, the distribution of C_f used in the region is in close agreement to previous studies. For example, Lefevre, Provost, and Lyard (2000) found a small value of C_f (1.5×10^{-3}) to be optimal throughout the East China Sea/Yellow Sea region. More interestingly the distribution of C_f closely resembles the optimal one determined through the adjoint method (Lu and Zhang, 2006). This may appear to indicate that the adjoint method can estimate C_f values that correspond to physical characteristics of the seabed such as the muddy nature throughout most of the Yellow Sea. However, it is not clear whether the sand zone south of the Yellow Sea creating an increase in C_f similar to the optimal distribution of C_f in Lu and Zhang (2006) was simply a coincidence or not due to the sparseness of data points in the census here and the tendency of sand zones in the other two regions to in fact increase discrepancies.

The Arafura Sea in the census is mainly fine-grained calcareous but there are two pockets of sand zones. However, according to the grain size map presented in Porter-Smith et al. (2004), we expect the Arafura Sea and Gulf of Carpentaria to be fairly muddy with small grain sizes. In the Timor Sea the census contains many data points that are used to determine that the sediment is sandy here. This may be the case, but our definition of the sediment grain size of sand does not seem to match Porter-Smith et al. (2004), which indicates fairly small grain sizes for the region. The rest of the Australian shelf has fairly large grain sizes (Porter-Smith et al., 2004), but they are mainly designated as ooze types in the census. It can be assumed that there are similar issues with sediment types and the correlation of these to physical sediment characteristics in the area between the Java Sea and South China Sea. This indicates that the census is generally insufficient for our purpose due to the relative sparseness of the data, particularly of terrestrial type sediments, and because it requires us to estimate the grain size and density from the sediment types. The physical characteristic of sand, for example, can vary considerably.

We have experimented with changing some of the sediment type definitions of the census. For example, the sandy sediment definition in the area between Java Sea and South China Sea was changed to fine-grained calcareous sediment which decreases the discrepancies around Singapore for

M_2. Similarly, all of the Arafura Sea was changed to a muddy sediment type and Timor Sea to fine-grained calcareous sediment (based on the grain size figure in Porter-Smith et al. (2004)). This led to generally improved results. In future studies if actual physical sediment characteristics from databases (e.g Porter-Smith et al., 2004; Buczkowski et al., 2006) could be adopted, with a focus on regions where R_f exceeds 0.4-0.5 in particular, there are indications that non-trivial improvements to tidal solutions can be achieved (e.g. Yellow Sea, Bohai Sea, and Seto Inland Sea).

6 Conclusions

This study presented a finite-element barotropic model of the Indian and Western Pacific Oceans with elemental resolution ranging from as small as 100 m (in Hong Kong) up to 25 km in less barotropically interesting areas of the deep ocean. Most of the resolution at the coast is 1 km. Bathymetry was sourced predominantly from the global SRTM bathymetric database in addition to local high-resolution datasets and hand-edits. We began by making comparisons with both the data-assimilated TPXO8 atlas and tidal constituents at tide gauges in deep, continental shelf and slope waters, and at the coast. This was followed by a presentation of the sensitivities to lateral boundary conditions, bathymetry, internal tide dissipation, and bottom friction dissipation. Within each of these sections a discussion of the findings and implications with regards to the sensitivity for that component was presented. The key results (e.g. RMS discrepancies for the *Comp + IT + SV* model setup) and conclusions for each region (deep, shelf, and coastal) follows.

Deep water M_2 mean RMS discrepancies against TPXO8 are 2.9 cm (RMSE = 3.6 cm) which is marginally better than reported for other forward hydrodynamic models. However, the total free surface RMS discrepancies at deep water tide gauges are 2.3 times those of the TPXO8 atlas. Poorly placed elevation specified lateral boundaries led to global resonant amplifications of the lunar semi-diurnal modes. An absorption-generation sponge zone suppressed the resonant amplifications but it relies on data-assimilated model fluxes (e.g. TPXO8 and similar models) which may not be as reliable as the elevations from these models. A comprehensive global forward model may have advantages in eliminating the uncertainties from the boundary conditions. Strictly bathymetric effects were not of great importance to the deep water solution, however internal tide dissipation (that relies on topographic features and slopes for parameterization) was shown to be the key control in deep water. The *Nycander* method for internal tide dissipation was shown to obtain marginally superior results to the *Directional* method, but the latter was more dissipative in the Indian Ocean and hence resulted in smaller M_2 amplitudes here (which match TPXO8 slightly better). There was evidence that there is scope to further improve the deep water solution through internal tide dissipation but it is probably not possible using the same paradigm (strict reliance on the *Nycander* equation and calibration of a global amplification factor) as presented here. Significant local modifications based on 3D baroclinic models and measurements, including improvements to internal tide dissipation in shallower waters are likely required.

Continental shelf and slope water M_2 mean RMS discrepancies against TPXO8 are 6.5 cm (RMSE = 10.1 cm). This was shown to be significantly superior to those reported for other forward hydrodynamic models (RMSE = 19-28 cm (Stammer et al., 2014), albeit these are global errors, the total energy density is at least as large in the IndWPac domain compared to the rest of the world's ocean). One of the most important factors for improvement was shown to be the inclusion of local high-resolution bathymetry. Notable changes in the M_2 amplitude and a corresponding reduction in the RMS discrepancies against TPXO8 and at tide gauges were evident in the greater Yellow Sea region due to changes in bottom friction coefficients based on combinations of muddy and sandy sediment types. However, the regions around the Java and South China Seas, and Timor and Ara-

fura Seas did not generate significant nor positive changes to the discrepancy. If more complete databases of physical characteristics of sediment are made available, combined with accurate local bathymetric data it may be possible to improve solutions elsewhere, particularly in resonant basins (e.g. Gulfs of Khambhat and Kutch on the west coast of India; King Sound, Joseph Bonaparte Gulf and Van Diemen Gulf in northern Australia, among others) due to spatially varying bottom friction coefficients. Nevertheless, we are still limited by residual discrepancies from deeper waters and the uncertainties of internal tide dissipation in shallower waters.

The discrepancies at the coast for the IndWPac model were not significantly different from those obtained further offshore on the shelf. Furthermore, the mean total free surface RMS discrepancies at coastal tide gauges ($\overline{D}_{tg} = 14$ cm) were 2.6 cm smaller than those of the TPOX8 atlas. However, the discrepancy at the majority of locations are smaller for the TPXO8 atlas due to data-assimilation offshore and at selected tide gauges. The large mean RMS discrepancy for the TPXO8 atlas is likely related to TPXO8's coarser resolution not resolving certain nearshore features and harbor complexes in detail and therefore not correctly propagating the tides into them. For example, bathymetric and bottom friction controls were both found to play a very important role nearshore, and in some cases dominate the reasons for discrepancy due to resonance in a basin or inadequate connectivity into a bay. In contrast, the IndWPac model does not have such a large number or magnitude of outlier locations. These results are an indication that the model adequately captures a large amount of the nearshore physics throughout the domain. Thus, the model is potentially suitable to simulate a great range of shallow water physics within the region, specifically into detailed harbor complexes and other nearshore features where the tide gauges are located.

If we are solely interested in tidal elevations, then the simple answer is to use data-assimilation within the IndWPac model to achieve highly accurate solutions, from the deep ocean all the way to the well-resolved coastal regions. However, in many other applications, such as the forecasting and analysis of coupled surge, tide and wave processes, capturing the large-scale responses to meteorology, and modeling the shallow water physics including the nonlinear interactions of the processes becomes vital. In order to accomplish this, correctly specifying high-resolution bathymetry and topography become controlling factors. Furthermore, physics based improvements to more accurately quantify dissipation within forward barotropic models are possible offshore, through coupling to coarser 3D baroclinic numerical models, and nearshore, through bottom bedform and sediment roughness data.

Acknowledgements

We are indebted to Professor Seungwon Suh from Kunsan National University for providing the computational grid and bathymetric data for the South Korean peninsula. We also thank Dr. Shintaro Bunya from Mitsubishi Research Institute, for providing the computational grid and bathymetric data for Tokyo Bay, and Dr. Patrick Timko from Bangor University for providing the SRTM30_PLUS bathymetry with synthetic abyssal hill roughness. In addition to the Office of Naval Research grant N00014-15-1-2623, the model development work was supported by Factory Mutual Insurance Company (FM Global), Norwood, MA. The development of the absorption-generation sponge layer was supported by the National Science Foundation under grant ACI-1339738.

References

Apecechea, Maialen Irazoqui et al. (2017). "Effects of self-attraction and loading at a regional scale: a test case for the Northwest European Shelf". In: *Ocean Dyn.* 67.6, pp. 729–749. DOI: 10.1007/s10236-017-1053-4.

Beaman, R J and P E O'Brien (2011). *Kerguelen Plateau Bathymetric Grid, November 2010.* Tech. rep. November. Canberra, Australia: Geoscience Australia, p. 18.

Beaman, Robin J (2010). *Project 3DGBR: A high-resolution depth model for the Great Barrier Reef and Coral Sea.* Tech. rep. June. Cairns. Australia: Marine and Tropical Sciences Research Facility (MTSRF), p. 13.

Becker, J. J. et al. (2009). "Global Bathymetry and Elevation Data at 30 Arc Seconds Resolution: SRTM30_PLUS". In: *Mar. Geod.* 32.4, pp. 355–371. DOI: 10.1080/01490410903297766.

Bilskie, Matthew V. and Scott C. Hagen (2013). "Topographic accuracy assessment of bare earth lidar-derived unstructured meshes". In: *Adv. Water Resour.* 52, pp. 165–177. DOI: 10.1016/j.advwatres.2012.09.003.

Buczkowski, B J et al. (2006). *usSEABED: Gulf of Mexico and Caribbean offshore surficial-sediment data release.* Tech. rep.

Buijsman, Maarten C. et al. (2014). "Three-Dimensional Double-Ridge Internal Tide Resonance in Luzon Strait". In: *J. Phys. Oceanogr.* 44.3, pp. 850–869. DOI: 10.1175/JPO-D-13-024.1.

Buijsman, M.C. et al. (2015). "Optimizing internal wave drag in a forward barotropic model with semidiurnal tides". In: *Ocean Model.* 85, pp. 42–55. DOI: 10.1016/j.ocemod.2014.11.003.

Bunya, S. et al. (2010). "A High-Resolution Coupled Riverine Flow, Tide, Wind, Wind Wave, and Storm Surge Model for Southern Louisiana and Mississippi. Part I: Model Development and Validation". In: *Mon. Weather Rev.* 138.2, pp. 345–377. DOI: 10.1175/2009MWR2906.1.

Caldwell, P C, M A Merrifield, and P R Thompson (2015). *Sea level measured by tide gauges from global oceans as part of the Joint Archive for Sea Level (JASL) from 1846-01-01 to 2015-07-31.* DOI: 10.7289/V5V40S7W.

Charnock, H. (1959). "Tidal Friction from Currents near the Seabed". In: *Geophys. J. Int.* 2.3, pp. 215–221. DOI: 10.1111/j.1365-246X.1959.tb05794.x.

Chassignet, Eric P. et al. (2007). "The HYCOM (HYbrid Coordinate Ocean Model) data assimilative system". In: *J. Mar. Syst.* 65.1-4, pp. 60–83. DOI: 10.1016/j.jmarsys.2005.09.016.

Codiga, Daniel L (2011). *Unified Tidal Analysis and Prediction Using the UTide Matlab Functions.* Tech. rep. 01. Narragansett, RI: Graduate School of Oceanography, University of Rhode Island, p. 59. DOI: 10.13140/RG.2.1.3761.2008.

Dresback, Kendra M., Randall L. Kolar, and Richard A. Luettich, Jr. (2005). "On the Form of the Momentum Equation and Lateral Stress Closure Law in Shallow Water Modeling". In: *Estuar. Coast. Model.* Reston, VA: American Society of Civil Engineers, pp. 399–418. ISBN: 978-0-7844-0876-6. DOI: 10.1061/40876(209)23.

Dutkiewicz, Adriana et al. (2015). "Census of seafloor sediments in the world's ocean". In: *Geology* 43.9, pp. 795–798. DOI: 10.1130/G36883.1.

Egbert, Gary D. and Svetlana Y. Erofeeva (2002). "Efficient Inverse Modeling of Barotropic Ocean Tides". In: *J. Atmos. Ocean. Technol.* 19.2, pp. 183–204. DOI: 10.1175/1520-0426(2002)019<0183:EIMOBO>2.0.CO;2.

Egbert, Gary D. and Richard D. Ray (2001). "Estimates of M2 tidal energy dissipation from TOPEX/Poseidon altimeter data". In: *J. Geophys. Res. Ocean.* 106.C10, pp. 22475–22502. DOI: 10.1029/2000JC000699.

Egbert, Gary D., Richard D. Ray, and Bruce G. Bills (2004). "Numerical modeling of the global semidiurnal tide in the present day and in the last glacial maximum". In: *J. Geophys. Res. Ocean.* 109.C3. DOI: 10.1029/2003JC001973.

Fang, Guohong et al. (1999). "Numerical simulation of principal tidal constituents in the South China Sea, Gulf of Tonkin and Gulf of Thailand". In: *Cont. Shelf Res.* 19.7, pp. 845–869. DOI: 10.1016/S0278-4343(99)00002-3.

Fang, Guohong et al. (2004). "Empirical cotidal charts of the Bohai, Yellow, and East China Seas from 10 years of TOPEX/Poseidon altimetry". In: *J. Geophys. Res. Ocean.* 109.11, pp. 1–13. DOI: 10.1029/2004JC002484.

Goff, John A. and Brian K. Arbic (2010). "Global prediction of abyssal hill roughness statistics for use in ocean models from digital maps of paleo-spreading rate, paleo-ridge orientation, and sediment thickness". In: *Ocean Model.* 32.1, pp. 36–43. DOI: 10.1016/j.ocemod.2009.10.001.

Green, J. A. Mattias and Jonas Nycander (2013). "A Comparison of Tidal Conversion Parameterizations for Tidal Models". In: *J. Phys. Oceanogr.* 43.1, pp. 104–119. DOI: 10.1175/JPO-D-12-023.1.

Green, J.A. Mattias and Tomos W. David (2013). "Non-assimilated tidal modeling of the South China Sea". In: *Deep Sea Res. Part I Oceanogr. Res. Pap.* 78, pp. 42–48. DOI: 10.1016/j.dsr.2013.04.006.

Heathershaw, A. D. (1979). "The turbulent structure of the bottom boundary layer in a tidal current". In: *Geophys. J. Int.* 58.2, pp. 395–430. DOI: 10.1111/j.1365-246X.1979.tb01032.x.

Heathershaw, A.D. and J.H. Simpson (1978). "The sampling variability of the Reynolds stress and its relation to boundary shear stress and drag coefficient measurements". In: *Estuar. Coast. Mar. Sci.* 6.3, pp. 263–274. DOI: 10.1016/0302-3524(78)90015-4.

Hendershott, M. C. (1972). "The Effects of Solid Earth Deformation on Global Ocean Tides". In: *Geophys. J. Int.* 29.4, pp. 389–402. DOI: 10.1111/j.1365-246X.1972.tb06167.x.

Jayne, Steven R. and Louis C. St. Laurent (2001). "Parameterizing tidal dissipation over rough topography". In: *Geophys. Res. Lett.* 28.5, pp. 811–814. DOI: 10.1029/2000GL012044.

Kerr, P. C. et al. (2013). "U.S. IOOS coastal and ocean modeling testbed: Evaluation of tide, wave, and hurricane surge response sensitivities to mesh resolution and friction in the Gulf of Mexico". In: *J. Geophys. Res. Ocean.* 118.9, pp. 4633–4661. DOI: 10.1002/jgrc.20305.

Krien, Y. et al. (2016). "Improved Bathymetric Dataset and Tidal Model for the Northern Bay of Bengal". In: *Mar. Geod.* 39.6, pp. 422–438. DOI: 10.1080/01490419.2016.1227405.

Le Provost, C and Florent Lyard (1997). "Energetics of the M2 barotropic ocean tides: an estimate of bottom friction dissipation from a hydrodynamic model". In: *Prog. Oceanogr.* 40.1, pp. 37–52. DOI: 10.1016/S0079-6611(97)00022-0.

Lefevre, Fabien, C Le Provost, and F H Lyard (2000). "How can we improve a global ocean tide model at a region scale? A test on the Yellow Sea and the East China Sea". In: *J. Geophys. Res. Ocean.* 105.C4, pp. 8707–8725. DOI: 10.1029/1999JC900281.

Lu, Xianqing and Jicai Zhang (2006). "Numerical study on spatially varying bottom friction coefficient of a 2D tidal model with adjoint method". In: *Cont. Shelf Res.* 26.16, pp. 1905–1923. DOI: 10.1016/j.csr.2006.06.007.

Lyard, Florent et al. (2006). "Modelling the global ocean tides: modern insights from FES2004". In: *Ocean Dyn.* 56.5-6, pp. 394–415. DOI: 10.1007/s10236-006-0086-x.

Matsumoto, Koji, Takashi Takanezawa, and Masatsugu Ooe (2000). "Ocean Tide Models Developed by Assimilating TOPEX/POSEIDON Altimeter Data into Hydrodynamical Model: A Global Model and a Regional Model around Japan". In: *J. Oceanogr.* 56.5, pp. 567–581. DOI: 10.1023/A:1011157212596.

Melet, Angélique et al. (2013). "Internal tide generation by abyssal hills using analytical theory". In: *J. Geophys. Res. Ocean.* 118.11, pp. 6303–6318. DOI: 10.1002/2013JC009212.

Ngodock, Hans E. et al. (2016). "On improving the accuracy of the M2 barotropic tides embedded in a high-resolution global ocean circulation model". In: *Ocean Model.* 97, pp. 16–26. DOI: 10.1016/j.ocemod.2015.10.011.

Nycander, J. (2005). "Generation of internal waves in the deep ocean by tides". In: *J. Geophys. Res.* 110.C10, p. C10028. DOI: 10.1029/2004JC002487.

Padman, Laurie et al. (2002). "A new tide model for the Antarctic ice shelves and seas". In: *Ann. Glaciol.* 34.1, pp. 247–254. DOI: 10.3189/172756402781817752.

Persson, Per-olof and Gilbert Strang (2004). "A Simple Mesh Generator in MATLAB". In: *SIAM Rev.* 46, p. 2004. DOI: 10.1137/S0036144503429121.

Porter-Smith, R. et al. (2004). "Classification of the Australian continental shelf based on predicted sediment threshold exceedance from tidal currents and swell waves". In: *Mar. Geol.* 211.1-2, pp. 1–20. DOI: 10.1016/J.MARGEO.2004.05.031.

Pringle, William J (2017). *Major tidal constituents for the Indian Ocean and Western Pacific Basin.* DOI: 10.17632/tjyjn56jbf.1.

Ray, R. D. (1998). "Ocean self-attraction and loading in numerical tidal models". In: *Mar. Geod.* 21.3, pp. 181–192. DOI: 10.1080/01490419809388134.

Rijn, Leo C. van (2007). "Unified View of Sediment Transport by Currents and Waves. I: Initiation of Motion, Bed Roughness, and Bed-Load Transport". In: *J. Hydraul. Eng.* 133.6, pp. 649–667. DOI: 10.1061/(ASCE)0733-9429(2007)133:6(649).

Robertson, Robin and Amy Ffield (2008). "Baroclinic tides in the Indonesian seas: Tidal fields and comparisons to observations". In: *J. Geophys. Res. Ocean.* 113.7, pp. 1–22. DOI: 10.1029/2007JC004677.

Sandwell, David T. et al. (2014). *SRTM15_PLUS: Data Fusion of SRTM Land Topography with Measured and Estimated Seafloor topography.*

Schlichting, Herrmann (1979). *Boundary-Layer Theory.* 7th ed. Springer International Publishing, p. 817.

Shum, C K et al. (1997). "Accuracy assessment of recent ocean tide models". In: *J. Geophys. Res. Ocean.* 102.C11, pp. 173–194. DOI: 10.1029/97JC00445.

Smagorinsky, J. (1963). "General Circulation Experiments with the Primitive Equations. I. The Basic Experiment". In: *Mon. Weather Rev.* 91.3, pp. 99–164. DOI: 10.1175/1520-0493(1963)091<0099:GCEWTP>2.3.CO;2.

Snyder, R. L., M. Sidjabat, and J. H. Filloux (1979). "A Study of Tides, Setup and Bottom Friction in a Shallow Semi-Enclosed Basin. Part II: Tidal Model and Comparison with Data". In: *J. Phys. Oceanogr.* 9.1, pp. 170–188. DOI: 10.1175/1520-0485(1979)009<0170:ASOTSA>2.0.CO;2.

Stammer, D. et al. (2014). "Accuracy assessment of global barotropic ocean tide models". In: *Rev. Geophys.* 52.3, pp. 243–282. DOI: 10.1002/2014RG000450.

Suh, Seung Won, Hwa Young Lee, and Hyeon Jeong Kim (2014). "Spatio-temporal variability of tidal asymmetry due to multiple coastal constructions along the west coast of Korea". In: *Estuar. Coast. Shelf Sci.* 151, pp. 336–346. DOI: 10.1016/j.ecss.2014.09.007.

TCarta Marine (2012). *Marine Global Bathymetric Model for (DBM) East Asia.*

Technology Riverside Inc. and AECOM (2015). *Mesh Development, Tidal Validation, and Hindcast Skill Asessment of an ADCIRC Model for the Hurricane Storm Surge Operational Forecast System on the US Gulf-Atlantic Coast.* Tech. rep. National Oceanic and Atmospheric Administration/Nation Ocean Service, Coast Survey Development Laboratory, Office of Coast Survey, p. 179. DOI: 10.7921/G0MC8X6V.

Timko, Patrick G. et al. (2017). "Impact of synthetic abyssal hill roughness on resolved motions in numerical global ocean tide models". In: *Ocean Model.* 112, pp. 1–16. DOI: 10.1016/j.ocemod.2017.02.005.

Wang, Xiaochun et al. (2012). "Comparison of two methods to assess ocean tide models". In: *J. Atmos. Ocean. Technol.* 29.8, pp. 1159–1167. DOI: 10.1175/JTECH-D-11-00166.1.

Weatherall, Pauline et al. (2015). "A new digital bathymetric model of the world's oceans". In: *Earth Sp. Sci.* 2, pp. 331–345. DOI: 10.1002/2015EA000107.

Wei, Zexun et al. (2016). "Tidal elevation, current, and energy flux in the area between the South China Sea and Java Sea". In: *Ocean Sci.* 12.2, pp. 517–531. DOI: 10.5194/os-12-517-2016.

Westerink, J. J. et al. (1992). "Tide and Storm Surge Predictions Using Finite Element Model". en. In: *J. Hydraul. Eng.* 118.10, pp. 1373–1390. DOI: 10.1061/(ASCE)0733-9429(1992)118:10(1373).

Westerink, Joannes J. et al. (2008). "A Basin- to Channel-Scale Unstructured Grid Hurricane Storm Surge Model Applied to Southern Louisiana". EN. In: *Mon. Weather Rev.* 136.3, pp. 833–864. DOI: 10.1175/2007MWR1946.1.

Whiteway, T. (2009). *Australian Bathymetry and Topography Grid, June 2009.* DOI: 10.4225/25/53D99B6581B9A.

Woodworth, P L et al. (2017). "Towards a global higher-frequency sea level dataset". In: *Geosci. Data J.* 3, pp. 50–59. DOI: 10.1002/gdj3.42.

You, Zai-Jin (2005). "Estimation of bed roughness from mean velocities measured at two levels near the seabed". In: *Cont. Shelf Res.* 25.9, pp. 1043–1051. DOI: 10.1016/j.csr.2005.01.001.

Zahel, Wilfried and Malte Müller (2005). "The computation of the free barotropic oscillations of a global ocean model including friction and loading effects". In: *Ocean Dyn.* 55.2, pp. 137–161. DOI: 10.1007/s10236-005-0029-y.

Zaron, Edward D. (2017). "Topographic and frictional controls on tides in the Sea of Okhotsk". In: *Ocean Model.* 117, pp. 1–11. DOI: 10.1016/j.ocemod.2017.06.011.

Zaron, Edward D. and Gary D. Egbert (2006). "Estimating Open-Ocean Barotropic Tidal Dissipation: The Hawaiian Ridge". In: *J. Phys. Oceanogr.* 36.6, pp. 1019–1035. DOI: 10.1175/JPO2878.1.

Zhang, Yao et al. (2014). "Generatingabsorbing sponge layers for phase-resolving wave models". In: *Coast. Eng.* 84, pp. 1–9. DOI: 10.1016/j.coastaleng.2013.10.019.

Zu, Tingting, Jianping Gan, and Svetlana Y. Erofeeva (2008). "Numerical study of the tide and tidal dynamics in the South China Sea". In: *Deep Sea Res. Part I Oceanogr. Res. Pap.* 55.2, pp. 137–154. DOI: 10.1016/j.dsr.2007.10.007.

A Effective Sediment Roughness Equations

The equations for the effective sediment roughness k_s are taken from Rijn (2007). k_s is calculated from the vector sum of roughnesses from the different bedform types:

$$k_s = \left(k_{s,r}^2 + k_{s,m}^2 + k_{s,d}^2\right)^{0.5} \tag{21}$$

where $k_{s,r}$, $k_{s,m}$, $k_{s,d}$ are the ripple, mega-ripple, and dune related roughnesses respectively. Equations for each rely on the current mobility parameter ψ:

$$\psi = \frac{u_f^2}{(s-1)gd_{50}} \tag{22}$$

where u_f is the effective mean current speed (7), $s = \rho_s/\rho_0$ is the relative sediment density (ρ_s is the sediment density), g is the acceleration due to gravity, and d_{50} is the median sediment grain diameter. The equations for each individual roughness type are then:

$$k_{s,r} = f_{sc} d_{50} \left(85 - 65 \tanh[0.015(\psi - 150)]\right) \tag{23}$$

$$k_{s,m} = \max\left(\min\left(0.02, 200d_{50}\right), 2e^{-5} f_{fs} h \left[1 - \exp(-0.05\psi)\right](550 - \psi)\right) \tag{24}$$

$$k_{s,d} = \max\left(0, 8e^{-5} f_{fs} h \left[1 - \exp(-0.02\psi)\right](600 - \psi)\right) \tag{25}$$

where h is the still water depth, f_{sc} is the "factor which expresses the effect of a gradually decreasing ripple roughness for very coarse sediment beds", and f_{fs} is the "factor which expresses the effect of a gradually decreasing mega-ripple roughness for very fine sediment beds" (Rijn, 2007):

$$f_{cs} = \min\left[1, \left(\frac{0.25 d_{grav}}{d_{50}}\right)^{1.5}\right] \tag{26}$$

$$f_{fs} = \min\left[1, \frac{d_{50}}{1.5 d_{sand}}\right] \tag{27}$$

where $d_{grav} = 2\times10^{-3}$ m, and $d_{sand} = 6.2\times10^{-5}$ m. Here, all sediments are assumed to have $d_{50} > d_{silt} = 3.2\times10^{-5}$ m, in which otherwise a lower limit of $k_s = 20 d_{silt}$ is applied.